# Integrated Photonics Structure for THz Systems Based on Silicon and Photoconductive Material

by

Sohrab Samiezadeh

A thesis
presented to the University of Waterloo
in fulfillment of the
thesis requirement for the degree of
Master of Applied Science
in
Electrical and Computer Engineering

Waterloo, Ontario, Canada, 2022

## Author’s Declaration

I hereby declare that I am the sole author of this thesis. This is a true copy of the thesis, including any required final revisions, as accepted by my examiners.

I understand that my thesis may be made electronically available to the public.

## Abstract

The field of terahertz (THz) technology has been immensely progressed over the past two decades, but integrated on-chip THz circuits and systems are still under development. This thesis is an effort to propose an integrated THz system by trapping a generated photocurrent THz wave and its coupling to the waveguide for on-chip propagation and processing. The proposed system consists of three parts; an optically-excited photoconductive THz source based on low-temperature grown (LT)-GaAs, a photonic crystal nanobeam cavity for THz wave confinement, and its coupling to a waveguide, both are based on a silicon platform.

The thesis first investigates how the THz signal is generated by the photomixing techniques. It presents an analytical model to calculate the time-varying photocurrent acting as a THz source. Considering the THz dipole current exciting a cavity, I propose a photonic crystal nanobeam cavity inside a waveguide with high quality factor to confine the THz wave. The design and simulation of such a cavity are presented where the THz field mode has been found in a single-mode regime. Finally, the cavity is coupled to the waveguide using a tapering technique in the photonic crystal structure for efficient coupling and subsequent propagation by modal field matching. The proposed structure exhibits potential applications for integrated THz sources for various on-chip applications such as sensing, spectroscopy, and signal processing.

## Acknowledgments

First of all, thank Allah for blessing me in every second of my life, especially the ones when I was working on my thesis and master's research.

I have started my studies under the supervision of an exceptional scientist, engineer, and above all, a great human, Professor Safieddin Safavi-Naeini. He was more than a supervisor to me, but unfortunately, he passed away in October 2021, before the end of my studies. I am so lucky to have had the chance of working with Professor Safavi-Naeini.

Special thanks to Professor Hamed Majedi, Professor Guo-Xing Miao, and Professor Pin-Han Ho for reading my thesis. I have also learned too much during my master's courses at UW, especially the Quantum course of Professor Majedi and the Numerical EM course of Professor Safavi-Naeini. Also, thanks to my bachelor's mentors, Professor Shahabadi and Professor Faraji-Dana for their comprehensive teaching in EM theory and supervision during my education at the University of Tehran.

Finally, thanks to my colleagues at CIARS, my roommates, and my friends in Canada and Iran, specially Mohsen and his family for inspiring me.

The most and the least, I am so merciful to my great family to be the main source of encouragement and support during my studies.

# Dedication

To my mother

To my father

To my grandmother

To my grandfather

To my brother

Finally, the least and the most:

To my darling wife, Nazanin Bahar

And her great family.

Thanks for your patience, emotional support, and endless love.

# Table of Contents

# List of Figures

# List of Tables

# Chapter 1
# Introduction

## 1.1 The Terahertz Gap

Terahertz (THz) compromises the range of frequencies between 100 GHz and 10 THz of the electromagnetic spectrum that lies between microwave and infrared light. The unique properties of THz waves can be used in many different applications in different areas such as data communications, biology, medical sciences, sensing, imaging, and spectroscopy.

THz waves penetrate deep into nonpolar and non-metallic materials like paper, wood, plastic, and clothes that are opaque at optical frequencies, and these are also common materials for packaging. Thus, THz imaging devices are used for non-destructive testing in hidden object detection, and in contrast to X-rays THz waves are non-ionizing and harmless for humans [3]. Furthermore, THz waves can be used for non-invasive medical and biological diagnostics instead of harmful X-rays.

THz waves have spectral features associated with fundamental physical processes like rotational transitions of molecules, large-amplitude vibrational motions of organic compounds, lattice vibrations in solids, and intraband transitions in semiconductors [3]. Hence, because of the physical fingerprints of materials in the THz domain, THz waves are a candidate for spectroscopy of materials. Also, because of the high atmospheric absorption and wide bandwidth of THz waves, they can be used for secure high-speed communication [2].

## 1.2 Research Motivation and Objectives

During the past two decades, the field of THz technology has grown in many different areas, from generation and guided propagation to control and detection. Despite the progress in this research area, an integrated structure for THz applications has not been matured yet. In the optical domain, integrated photonics is the leading research area for producing on-chip systems for different applications,

and in the microwave region and electronics (in the frequency range of less than 500 MHz), integrated circuit platforms are leading the on-chip applications. The THz domain is the frequency range between the microwave and infrared, thus researchers are working in both technologies in optics and microwave to find a suitable platform for integrated THz systems. In recent years, interest in silicon photonics systems is growing because of their potential to provide an on-chip structure with both electronics and photonics components in the same chip based on the silicon platform. Silicon photonics is compatible with industrial CMOS technologies that enable high-volume production for a low cost per device [1, 3].

The motivation of this thesis research is an effort to construct an integrated platform for THz applications that inspired me to research different parts of THz systems to find the most suitable components for providing an on-chip THz system.

The objective of this thesis is to propose a new method for the THz wave confinement using an integration of a photoconductive source with a photonic crystal nanobeam cavity.

The thesis is structured as in Figure 1-1. After a review of different generation methods and different confinement techniques, THz photoconductive source is chosen as the source of THz wave source, and a high-resistivity silicon (HR-Si) waveguide and nanobeam cavity are the final choices for confining and trapping the generated THz wave.

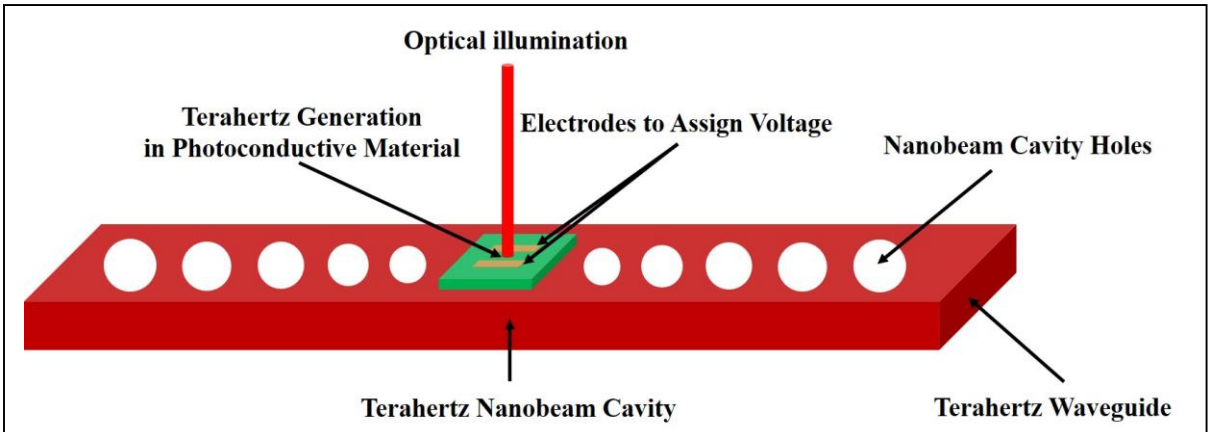


**Figure 1-1 Structure of the thesis**

As shown in Figure 1-1, this thesis describes many physical phenomena, including the interaction of incident optical waves with a photoconductive semiconductor to generate electron-hole pair carriers, assigning a DC voltage to carriers for movement of electrons to generate a generate THz wave, coupling to the cavity and its transitional coupling and subsequent propagation in the waveguide. The details of the different parts can be summarized thus:

1. Generating a THz photocurrent via optical excitation of voltage-biased photoconductive material through photomixing technique.
2. Design of the high-quality THz cavity to confine the generated photocurrent THz wave.
3. Efficient coupling of THz cavity to the guided wave for on-chip signal propagation.

No commercial software was able to simulate the whole structure because of the different Physics involved in this project, so my approach has been to break down the problem into different parts and then address each of them separately.

## 1.3 Thesis Outline and Contributions

As discussed above, the chapters of this thesis are defined by the approach of breaking down the initial complicated physical structures into different physical mechanisms, and then discussing the contribution of each part independently. Figure 1-2 shows the break down and corresponding thesis chapters.

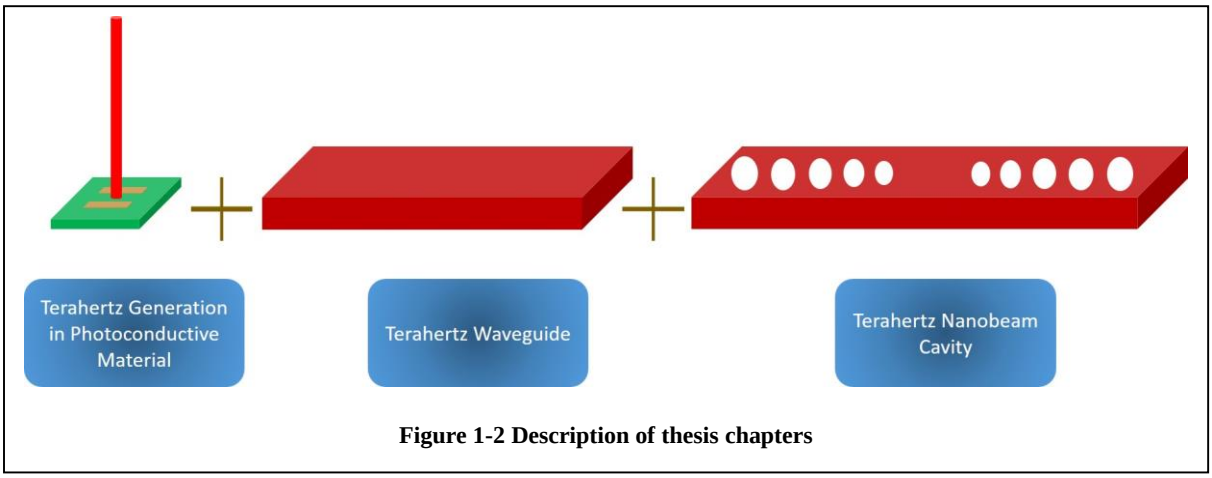


**Figure 1-2 Description of thesis chapters**

In Chapter 2, after a short review of different THz generation methods, photoconductive sources are chosen for THz generation and excitation of the THz waveguide in the THz nanobeam cavity. My contribution in this chapter is solving the equations relative to the interaction of light and the photoconductive semiconductor under special circumstances, and providing a simple model for the generated photocurrent.

In Chapter 3, different THz waveguide technologies are reviewed, their properties are compared, and a suspended HR-Si waveguide structure is chosen for the structure of the waveguide. My contribution in this chapter is defining, simulating, and analyzing a waveguide for the frequency of 1 THz. The modes of the waveguide have been defined with the same approach used for optical waveguides but for the THz structures.

Chapter 4 provides the main objective of this thesis, THz wave confinement in an integrated cavity with a photoconductive source. This chapter starts by reviewing high quality factor cavities and then focuses on photonic crystal nanobeam cavities. My contribution in this chapter is designing, simulating, and analyzing a high quality factor nanobeam cavity for 1 THz with excitation from the center of the cavity. The field is trapped inside this cavity, and the resonance mode at 1 THz is the same as the fundamental mode of the waveguide, so this structure is suitable for further coupling of the field to the waveguide.

# Chapter 2

# Terahertz Source Generation

This chapter briefly reviews different methods of THz generation, but the main focus is on photoconductive-based THz generation. A simple electric dipole model for a photoconductive current excited by pulsed laser or continuous-wave (CW) laser is developed. The dependence of this current on the relative parameters is discussed to identify an appropriate photoconductive source structure for exciting the on-chip structure (THz waveguide, or THz cavity). Finally, the properties of a photocurrent generated for both CW and the pulsed photocurrent are studied.

## 2.1 Introduction

The most challenging part of THz technology is constructing an efficient and compact source, and that is why this band is called the THz gap [3]. The THz gap is like a bridge between microwaves and infrared, and there are several different methods in electronics, photonics, and electron beam structures for its generation.

The main concern in source generation is the output power, volume, and compatibility with on-chip and fiber-based THz structures. As shown in Figure 2-1, for the frequencies near microwaves, electronics-based sources are more cost-effective, can provide appropriate output power, and are compatible with integrated circuit (IC) structures. For the higher frequencies near the infrared (IR), the photonics-based structures are more suitable, having more output power since the power of electronics sources decreases rapidly at high frequencies. Electron beam sources have very high power but are almost always huge, bulky structures that are expensive.

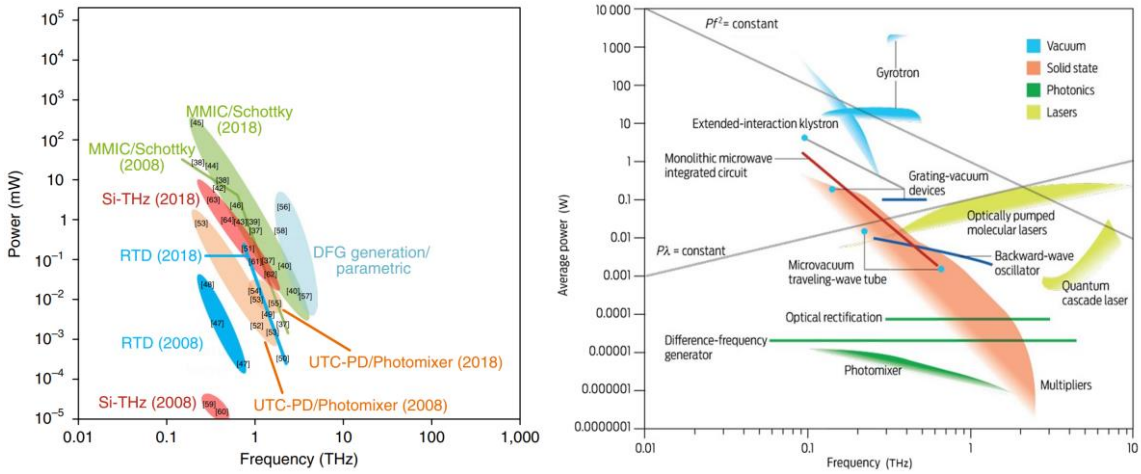


**Figure 2-1 (a) Progress of THz sources in the past decade showing how a selected set of integrated THz technologies has evolved over the past ten years in their ability to generate continuous-wave THz signals at room temperature. [4] (b) Power performance of conventional coherent tunable sources. [5]**

### 2.1.1 Direct Generation of THz

In this method, based on different physical methods, the output is a source working in the THz domain. Most of these structures are based on vacuum electron beams--huge structures such as backward-wave oscillators, free-electron lasers, gas lasers--and there are also quantum cascade lasers working in the THz regime.

Backward-wave oscillators (BWOs) produce THz waves based on the interaction of electron beams with a slow-wave structure. They can be electronically tuned by changing the acceleration voltage from sub-THz to 1.5 THz, and they can generate more than 50 mW of power at 0.3 THz going down to a few mW at 1 THz [3, 5, 6].

Free-electron lasers (FELs) generate coherent radiation by moving very high-speed electrons from periodic magnetic structures. Their output covers mainly the whole electromagnetic spectrum from microwaves to X-rays, and their output power can be very high--for instance, 1 KW at 0.3 THz [3, 6].

Gas lasers work based on pumping polar gas molecules lase on the THz frequency by means of infrared lasers. They can generate CW THz sources with an output power of up to 100 mW [3,6].

Quantum cascade lasers (QCLs) are unipolar semiconductor lasers based on intersubband (inside valance or conduction bands) transitions in structures like GaAs/AlGaAs. These structures are compact, but their tunability over a broadband frequency is challenging, as is obtaining the low-temperature required for working, which needs cryogenic cooling [3,6].

### 2.1.2 THz Generation via Up-conversion of Lower Frequencies

In this method, a chain of multipliers is required to up-convert the initial microwave or millimeter-wave (mm-wave) signal to the THz region. Using III-V-based structures such as InP heterojunction bipolar transistors (HBTs), GaAs Schottky diodes, and high electron mobility transistors (HEMTs) can generate a power level of 100 μW-mW in the THz and mm-wave frequency bands [4].

### 2.1.3 THz Generation via Down-conversion of Higher Frequencies

This case is based on using a nonlinear medium to generate the output THz signal by mixing the input optical pulses. The nonlinear media could be a second-order or third-order nonlinear material, and the output could be a broadband THz pulse or CW terahertz wave. THz pulses are generated based on optical rectification, $\chi^2_{(0,\omega,-\omega)}$, in second-order nonlinear materials such as lithium niobate excited by a femtosecond laser [19]. The first method used to generate THz CW wave relies on difference-frequency generation methods in a nonlinear medium, $\chi^2_{(\omega_{THZ},\omega_1,-\omega_2)}$ which is excited by two coherent lasers with the same polarization and frequency differences in the THz. The other method for CW THz generation is based on soliton microcomb by four-wave mixing (FWM) in a third-order nonlinear material like silica with a repetition rate in the THz regime [20]. The main disadvantage of this method is its lower output power because of the weak photon created in THz by

annihilating two large optical photons, so its conversion rate is in the order of $10^{-3}$ to $10^{-6}$.

### 2.1.4 THz Generation via Photoconductive material

In this case, optical illumination causes the generation of electron-hole carrier pairs inside a photoconductive material, and if a DC voltage is applied across two electrodes, the carriers start to move, and a photocurrent generates. This approach generates both pulse and CW THz waves based on optical illumination. The main focus of the thesis is based on this method, so its details are discussed further in the next sections.

## 2.2 Terahertz Photoconductive-Based Sources

Terahertz generation via photoconductivity of materials is one of the most famous methods based on the photomixing or heterodyning technique. This method can can generate a pulsed THz or CW THz wave based on the incident optical wave and a DC bias between two electrodes.

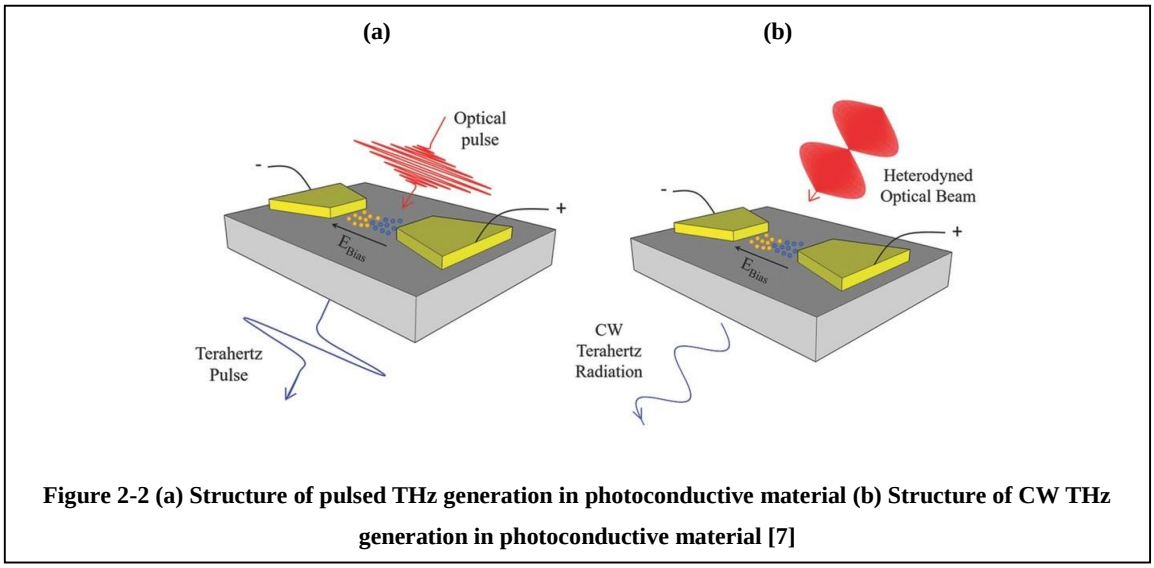


**Figure 2-2 (a) Structure of pulsed THz generation in photoconductive material (b) Structure of CW THz generation in photoconductive material [7]**

As shown in Figure 2-2, generating the THz wave requires that an incident optical wave generates the electron-hole pair carriers. The wavelength of the

incident wave must be near the bandgap of a photoconductive semiconductor material to excite electrons from the valance band to the conductance band. For this method, the most famous material is GaAs with a 1.424 eV (871 nm) bandgap. Another common material is InGaAs with 0.8 eV (1.55 μm) [8]. The photoconductive material should have a short carrier lifetime, high carrier mobility, and a large electrical field break-down to generate a THz wave with enough power [9]. Low temperature grown GaAs (LT-GaAs), which is grown by molecular beam epitaxy at a low substrate temperature (∼200 ℃) with a subpicosecond lifetime, ∼100 fs to ∼300 fs shortest reached lifetime, is the most common material employed in these systems [8], [9], [10], [21]. The generated carriers move by the force of the applied DC electric field relative to the DC-biased voltage. It is obvious that the output power increases when the power of incident optics or DC voltage bias is increased, thus the breakdown voltage of the material used should be high enough to tolerate the high DC electric field.

The material employed in the whole system investigated in this thesis is LT-GaAs because of its higher mobility, shorter lifetime, and higher breakdown electric field, thus the rest of this section focuses on LT-GaAs for THz generation.

By applying femtosecond optical pulses with a repetition rate in the microwave range, which is much longer than the duration of the optical pulse, this pulse acts as a switch for the DC bias and causes an output broadband THz pulse.

By applying a dual-mode CW laser or two CW lasers with the same polarization and difference frequency or beat frequency in THz, the gap between electrodes can be modeled as a modulated resistance with the beat frequency in THz. Thus, the output of this system would be a DC current and a current with THz frequency that generates a CW wave in THz with the beat frequency of lasers.

For physical modeling to find the output photocurrent, there are two methods. The first method, which is the main focus of the thesis, is based on semiconductor

equations, which can elaborate on the right amplitude and time evolution of the photocurrent. The second method is used in several of the most-cited references such as [10] and [11] and can only justify the time evolution of the photocurrent and explain the physical phenomena, but the amplitude is not found. The next sub-sections explain the details of each method.

### 2.2.1 1st Method of Theoretical Modeling for Photocurrent

This approach is based on the semiconductor equations in [9] and [12]. The electron-hole carrier pairs are generated by illuminating an optical electric field with the wavelength near the bandgap of the photoconductive material, LT-GaAs here. By applying a DC voltage bias across the electrodes, the carriers start to move and a photocurrent generates.

$$\vec{\nabla}.\left(\epsilon\vec{\nabla}\phi\right) = -e(p - n + N_D^+ - N_A^-) \quad (2.1)$$

$$\frac{\partial n}{\partial t} = G_n - R_n + \frac{1}{e}\vec{\nabla}.\overrightarrow{J_n} \quad (2.2)$$

$$\frac{\partial p}{\partial t} = G_p - R_p - \frac{1}{e}\vec{\nabla}.\overrightarrow{J_p} \quad (2.3)$$

$$\overrightarrow{J_n} = -e\mu_n n\vec{\nabla}\phi + eD_n\vec{\nabla}n \quad (2.4)$$

$$\overrightarrow{J_p} = -e\mu_p n\vec{\nabla}\phi - eD_p\vec{\nabla}p \quad (2.5)$$

$$G_n = G_p = \alpha\frac{I_{optical}}{h\nu} \quad (2.6)$$

$$R_n = -\frac{n}{\tau_{rn}} \qquad R_p = -\frac{p}{\tau_{rp}} \quad (2.7)$$

Equation (2.1) is Poisson's equation for a time-invariant electric potential, $\phi$ is the electrostatic potential, $e$ is the charge of an electron, $n$ and $p$ are electron and hole densities, $\epsilon$ is the permittivity of photoconductive material, $N_D^+$ is ionized donor concentration, and $N_A^-$ is the ionized acceptor concentration. Since the

movement of carriers is based on the DC voltage that causes a huge DC electric field, it is reasonable to ignore the time-variant fields which are orders of magnitude smaller than the DC electric field in the equations (2.4) and (2.5), and just solve the Poisson's equation for DC electrostatic potential. In (2.2) to (2.7), $G_n$ and $G_p$ are generation rates of electrons and holes, $R_n$ and $R_p$ are recombination rates of electron and hole, $J_n$ and $J_p$ are electron and hole current densities, $\mu_n$ and $\mu_p$ are electron and hole mobility, $D_n$ and $D_p$ are electron and hole diffusion coefficients, $\alpha$ is the absorption coefficient, $h$ is Plank's constant, $I_{optical}$ is optical intensity, $\nu$ is optical frequency, and $\tau_{rn}$ and $\tau_{rp}$ are electron and hole lifetimes. To simplify the equations for a dipole output current the DC field is approximated by a constant field between electrodes ($-\vec{\nabla}\phi = E_{DC}$) and the spatial variant of electrons and holes has been discarded ($\frac{\partial}{\partial x} = \frac{\partial}{\partial y} = \frac{\partial}{\partial z} = 0$) since the distance of electrodes is too much smaller than THz wavelength ($d \ll \lambda_{THz}$) and the output current is a simple dipole. Also, the lifetime of electrons and holes are the same ($\tau_{rn} = \tau_{rp} = \tau_r$).

$$\frac{\partial n}{\partial t} = -\frac{n}{\tau_r} + \alpha \frac{I_{optical}}{h\nu} \rightarrow\ n(t) = \frac{\alpha}{h\nu} e^{-\frac{t}{\tau_r}} \int_0^t e^{\frac{t'}{\tau_r}} I_{optical}(t')dt' \quad (2.8)$$

$$\frac{\partial p}{\partial t} = -\frac{p}{\tau_r} + \alpha \frac{I_{optical}}{h\nu} \rightarrow\ p(t) = \frac{\alpha}{h\nu} e^{-\frac{t}{\tau_r}} \int_0^t e^{\frac{t'}{\tau_r}} I_{optical}(t')dt' \quad (2.9)$$

$$J(t) = J_n(t) + J_p(t) = eE_{DC}\left(\mu_n n + \mu_p p\right) \quad (2.10)$$

The difference between pulsed and CW output THz waves is based on the input optical excitation. In pulsed systems, excitation is a Gaussian femtosecond optical pulse with the repetition rate in the microwave regime (~100 MHz) and a duration of $2\sqrt{\ln(2)}\,\tau_p$ [10].

$$I_{optical} = I_0 e^{-\frac{t^2}{\tau_p^2}} \quad (2.11)$$

In CW systems, the input is the summation of two CW optical waves with the same polarization ($\hat{p}$) and beat frequency of THz.

$$\vec{E}_{optical} = (E_1 \cos(\omega_1 t + \phi_1) + E_2 \cos(\omega_2 t + \phi_2))\, \hat{p} \quad (2.12)$$

$$I_{optical} = \langle \frac{1}{\eta_0} E_{optical}^2 \rangle_{T_{optical}}$$

$$I_{optical} = \frac{1}{\eta_0} \langle E_1^2 \cos^2(\omega_1 t + \phi_1) + E_2^2 \cos^2(\omega_2 t + \phi_2) + 2E_1 E_2 \cos(\omega_1 t + \phi_1) \cos(\omega_2 t + \phi_2) \rangle_{T_{optical}}$$

$$= \frac{1}{2\eta_0} E_1^2 + \frac{1}{2\eta_0} E_2^2 + \frac{E_1 E_2}{\eta_0} \cos(\omega_{THz} t + \phi_0)$$

$$I_{optical} = I_1 + I_2 + 2\sqrt{I_1 I_2} cos(\omega_{THz} t + \phi_0) \quad (2.13)$$

In (2.13), $\phi_0 = \phi_2 - \phi_1$ is the initial phase difference of optical waves, $\omega_{THz} = \omega_2 - \omega_1$ is the beat frequency of the incident optical waves, and $T_{optical}$ is the period of optical beams.

By replacing (2.11) and (2.13) in (2.8) to (2.10), the photocurrent density can be found as a function of time for the pulsed and CW systems in (2.14) and (2.15) respectively.

$$\boldsymbol{J^{pulse}(t) = \frac{\sqrt{\pi}\alpha I_0 \tau_p e E_{DC}}{2h\nu} (\mu_n + \mu_p) e^{-\left(\frac{t}{\tau_r} - \frac{\tau_p^2}{4\tau_r^2}\right)} \left( \mathbf{erf}\left(\frac{\tau_p}{\tau_r}\right) + \mathbf{erf}\left(\frac{t}{\tau_p} - \frac{\tau_p}{2\tau_r}\right)\right)} \quad \boldsymbol{(2.14)}$$

$$\boldsymbol{J^{CW}(t) = \frac{\alpha e E_{DC} \tau_r}{h\nu} (\mu_n + \mu_p) \left[ (I_1 + I_2)\left(1 - e^{-\frac{t}{\tau_r}}\right) + \frac{2\sqrt{I_1 I_2}}{\sqrt{1 + \omega_{THz}^2 \tau_r^2}} \left( \cos(\omega_{THz} t + \phi_0 - \phi_r) - \cos(\phi_0 - \phi_r)\, e^{-\frac{t}{\tau_r}} \right) \right]} \quad \boldsymbol{(2.15)}$$

This approach predicts the time evolution and the amplitude of the generated THz photocurrent. In (2.15), $\phi_r = \tan^{-1} \omega_{THz}\tau_r$.

### 2.2.2 2nd Method of Theoretical Modeling for Photocurrent

This method, which has been mentioned in important references in THz science such as [10], [11], and [22], is just a method to predict the time evolution of photocurrents. Here the method is explained in more detail than in the references, and the discarded coefficient is investigated to find the right amplitude in addition to the time evolution of the photocurrent.

To find out the output current, the photoconductive system is assumed to be a linear time-variant (LTI) system, and the first step is finding the impulse response of this system. The input of this LTI system is an optical beam, and its output is a generated photocurrent. The system is describing the movement of electrons in a DC electric field. The response of the system is the movement of generated electrons in one dimension, so first, the number of electrons, $n(t)$, generated by an impulse is found in equation (2.16). The generated electrons have a lifetime of $\tau_r$.

$$\frac{dn}{dt} = -\frac{n}{\tau_r} + \delta(t) \rightarrow n(t) = e^{-\frac{t}{\tau_r}}u(t) \quad (2.16)$$

To describe the movement, the equation of motion in one dimension, the direction of the gap between electrodes, for each electron with an effective mass of $m_e$ inside the photoconductive material based on the Drude-Lorentz model with a momentum relaxation time of $\tau_s$ and a DC biased electric field, $E_{DC}$, is solved in (2.17).

$$\frac{dv}{dt} = -\frac{v}{\tau_s} + \frac{e}{m_e}E_{DC} \rightarrow v(t) = \frac{e\tau_s}{m_e}E_{DC}\left(1 - e^{-\frac{t}{\tau_s}}\right)u(t) \quad (2.17)$$

The response of the system is moving $n(t)$ number of electrons with the velocity of $v(t)$ and charge of $e$; hence, the response of the system is relative to $en(t)v(t)$, but there should be a coefficient which cannot be identified here ($\kappa$). Hence the

response of the system is $\kappa e n(t) v(t)$. The output photocurrent is the convolution of the input optical pulse and response of the system, $H(t) = e n(t) v(t)$, and has been found in (2.18)

$$I_{PC}(t) = \int_0^\infty I_{optical}(t-\tau) H(\tau) d\tau = \int_0^\infty I_{optical}(t-\tau)[\kappa e n(\tau) v(\tau)] d\tau \quad (2.18)$$

By replacing (2.11), (2.13), (2.16), and (2.17) in (2.18), the output photocurrent for pulsed systems and CW systems is calculated in (2.19) and (2.20) respectively.

$$\boldsymbol{I_{PC}^{pulse} = I_A^{pulse}\left[e^{\frac{\tau_p^2}{4\tau_r^2}-\frac{t}{\tau_r}}\left(\mathbf{1}-\mathbf{erf}\left(\frac{\tau_p}{2\tau_r}-\frac{t}{\tau_p}\right)\right)-e^{\frac{\tau_p^2}{4\tau_{rs}^2}-\frac{t}{\tau_{rs}}}\left(\mathbf{1}-\mathbf{erf}\left(\frac{\tau_p}{2\tau_{rs}}-\frac{t}{\tau_p}\right)\right)\right]} \quad \mathbf{(2.19)}$$

$$\boldsymbol{I_{PC}^{CW} = I_D + \frac{I_{A_n}}{\sqrt{1+\omega_{THz}^2\tau_r^2}}\cos(\omega_{THz}t - \phi_r + \phi_0)}$$

$$\boldsymbol{+\frac{I_{A_{ns}}}{\sqrt{1+\omega_{THz}^2\tau_{rs}^2}}\cos(\omega_{THz}t - \phi_{rs} + \phi_0)} \quad \mathbf{(2.20)}$$

In (2.19) and (2.20), $\frac{1}{\tau_{rs}} = \frac{1}{\tau_r} + \frac{1}{\tau_s}$, $I_A^{pulse} = \frac{\sqrt{\pi}}{2}\kappa\frac{e^2\tau_s}{m_e}\tau_p E_{DC} I_0$, $I_D = \kappa(\tau_r + \tau_{rs})\frac{e^2\tau_s}{m_e}E_{DC}(I_1 + I_2)$, $I_{A_n} = 2\kappa\sqrt{I_1 I_2}\tau_r\frac{e^2\tau_s}{m_e}E_{DC}$, $\phi_r = \tan^{-1}\omega_{THz}\tau_r$, $I_{A_{ns}} = 2\kappa\sqrt{I_1 I_2}\tau_{rs}\mu_e e E_{DC}$, and $\phi_{rs} = \tan^{-1}\omega_{THz}\tau_{rs}$ are the renamed constants relative to the physical constants of the system.

By comparing the two methods in the next sub-chapter, the difference of time evolution of systems is discussed and the coefficient of response, $\kappa$, has been found.

### 2.2.3 Comparison of Two Modeling Methods

As discussed in the previous sub-sections, the second approach just identifies the time evolution of photocurrents, so for their comparison, just their temporal evolution is compared.

The numbers in [8] and [10] are used for LT-GaAs, which is the most common material in these systems, $\tau_s = 0.03\,ps$, and $\tau_r = 0.3\,ps$. The optical pulse width is 75 fs which is the number for the Chameleon Vision-S laser from the Coherent company and is used in the CIARS THz lab for the TDS setup ($\tau_p = \frac{75}{2\sqrt{\ln(2)}} \cong$ 45 fs). Using these numbers for the pulsed photocurrent and two optical beams in 870nm with the same intensity and difference frequency of 1THz for the CW photocurrent shows the comparison of the photocurrent's time evolution in the following figures.

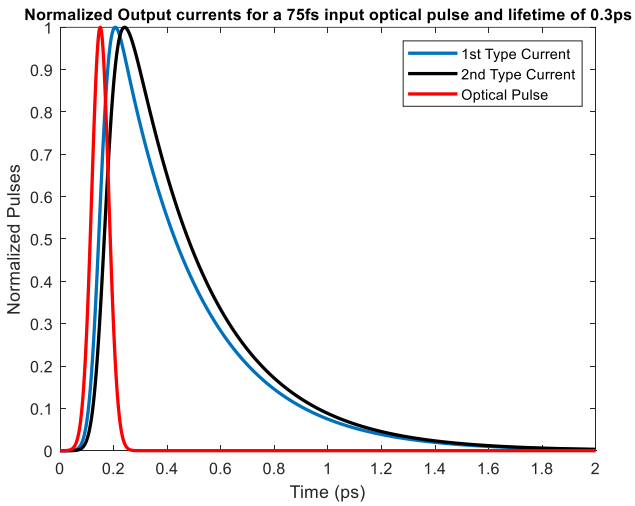


**Figure 2-3 75fs incident optical pulse at 870 nm and output current for different methods for THz pulse generation**

As shown in Figure 2-3, the time evolution is very similar for both methods. The second method has the accuracy of momentum relaxation in the order of 0.035ps in the order of momentum relaxation time, 0.03ps, and is negligible because it is too smaller than a carrier's lifetime (0.3ps).

For pulsed photocurrent, in the beginning, the photocurrent follows the optical pulse by just a delay relative to the delay of the response of the material, but after the optical pulse starts to decrease, the recombination time of the material ($\tau_r$)

causes a much slower response. since it is in the order of picoseconds, the generated current and wave are in the THz regime at the frequency domain.

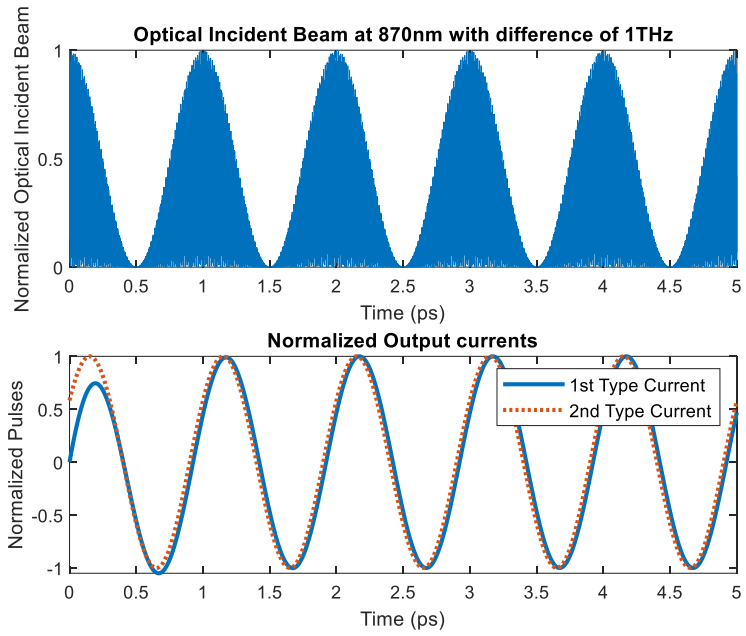


**Figure 2-4 Optical beam at 870 nm with modulation of 1THz and output current for different methods for THz CW generation**

As shown in Figure 2-4, again the time evolution is very similar for both methods. The second method's accuracy is in the order of 0.02ps because of the momentum relaxation, 0.03ps, and is negligible because it is much smaller than a carrier's lifetime (0.3ps). The other difference in CW generation is the transient part of the photocurrent at the beginning of the optical illumination, which is found only in the first approach and is not a matter of concern since will be disappeared after a very short time ($\tau_r$).

For the CW photocurrent, there is always a delay between the modulated optical beam and photocurrent because of the response time of the material ($\tau_r$), and it has been determined as $\tan^{-1}(\omega_{THz}\tau_r)$.

To estimate the coefficient of response in the second approach, $\kappa$, by discarding the momentum relaxation just in the time evolution of photocurrent and comparing equation (2.19) to (2.14) and (2.20) to (2.15), and assuming an effective area of $\Delta S$ for the movement of current density of the photocurrent there could be an approximation for the coefficient, $\kappa$, which has not been mentioned in the references such as [8].

$$\kappa = \frac{\alpha}{h\nu}\frac{m_e}{e\tau_s}(\mu_n + \mu_p)\Delta S \quad (2.21)$$

This coefficient determines the amplitude of a photoconductive material's response and is based on the specification of material $(m_e, \tau_s, \mu_n, \mu_p)$, optical illumination frequency $(\nu)$, and the geometry of the structure $(\alpha, \Delta S)$. For GaAs $m_e = 0.067m_0$, and $m_0$ is the mass of the electron.

## 2.3 Photocurrent Properties

This section focuses on the dependence of photocurrents on different properties of materials and incident beams. First, the properties of the pulsed THz wave and then the properties of the CW THz wave will be determined.

As discussed in Appendix A of this thesis and [11] and [13], the radiated far-field wave is relative to $\frac{\partial}{\partial t}J_{PC}(t)$, and the near-field, which couples to waveguides, cavities, etc., is relative to $J_{PC}$. Thus, the properties mentioned in [8], [9], and [13] are collected in Table 2-1, the output current and its properties for a pulsed system and a 1THz CW system will be shown in the following figures and discussed.

| $\tau_r$ | $\tau_p$ | $I_0$ | $\alpha$ | $E_{DC}$ | $\nu$ | $\mu_n$ | $\mu_p$ |
|---|---|---|---|---|---|---|---|
| 0.3 ps | 45 fs | $0.4\ \frac{mW}{\mu m^2}$ | $10^4\ \frac{1}{cm}$ | $2\times10^6\ \frac{v}{m}$ | 375 THz | $2\times10^4\ \frac{cm^2}{Vs}$ | $50\ \frac{cm^2}{Vs}$ |

**Table 2-1 Properties of a photoconductive pulsed system**

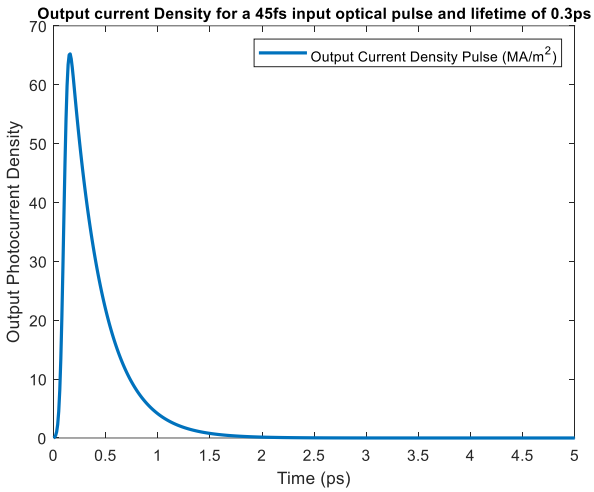


**Figure 2-5 Photocurrent Density of a pulsed system with properties in table 2-1**

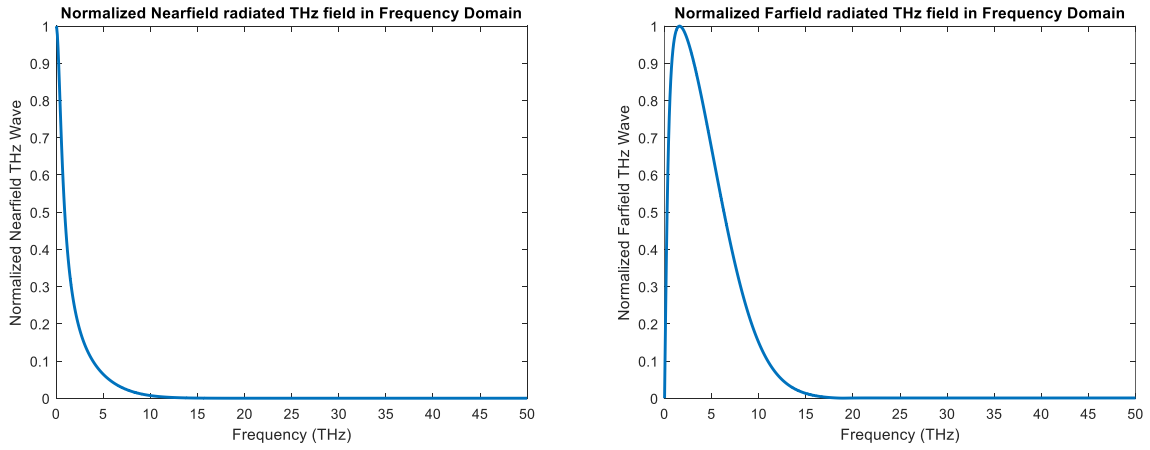


**Figure 2-6 Near-field and far-field THz wave in frequency domain**

The amplitude of the photocurrent is in the order of $\frac{MA}{m^2}$, but the output current would relative to the density and the effective cross-section area of the current, and this number is relative to the length of electrodes ($l$) and the depth of penetration of carriers inside the material ($d$). Due to the numbers in [8], [10], [15], and [16] they both are in the regime of $\mu m$ ($\Delta S = ld \sim \mu m^2$) so the current would be in the order

of $\mu A$ which also has been investigated in [16]. In [8], [15], and [16] the output current varies from $nA$ to $\mu A$, and this is because of different numbers for LT-GaAs mobility and penetration depth relative to the process of growth, size of the gap, absorption coefficient relative to the geometry of the structure, and the DC bias voltage. Compared to these references, this output current is reasonable and a very good simple model. The radiated electric field radiated with these properties has a bandwidth of near 520 GHz for near-field and 4.25 THz (0.45-4.7 THz) for the far-field region. Since the far-field wave has a wide range of frequencies, this method is used in terahertz time-domain spectroscopy (TDS) systems that a wide range of frequencies is needed to characterize materials by spectroscopy.

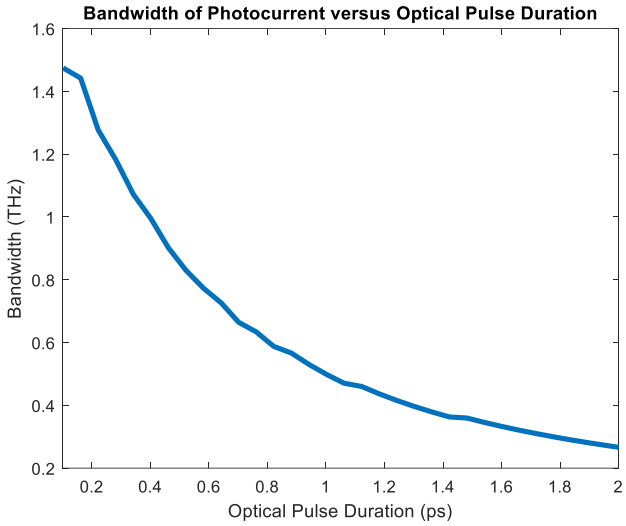


**Figure 2-7 Bandwidth of photocurrent pulse with different optical pulse durations for a lifetime of $\tau_r = 0.1\ ps$**

The bandwidth of output is relative $\tau_r$ and $\tau_p$. One of the initial ideas about this project was providing an on-chip TDS system, and the main concern was with the input optical beam, which needs a bulky expensive femtosecond laser. To resolve this issue, the idea was to compress a less expensive pulsed laser with a duration of

near $10ps$ with nonlinear optics methods like on-chip self-phase modulation on silicon [17], using two-photon absorption in a slow-wave waveguide [18], or other methods. However, these methods can compress the picosecond pulse by a factor maximum about 10, thus compressing the laser just in the order of picoseconds. For on-chip structure, the radiated field would be in the near-field regime, so due to Figure 2-6, the bandwidth of this system for optical pulses after 0.4ps is low, and the system has no special benefit. Thus, the idea of pulse compression for an on-chip TDS system was found not reasonable due to the properties and structures discussed above.

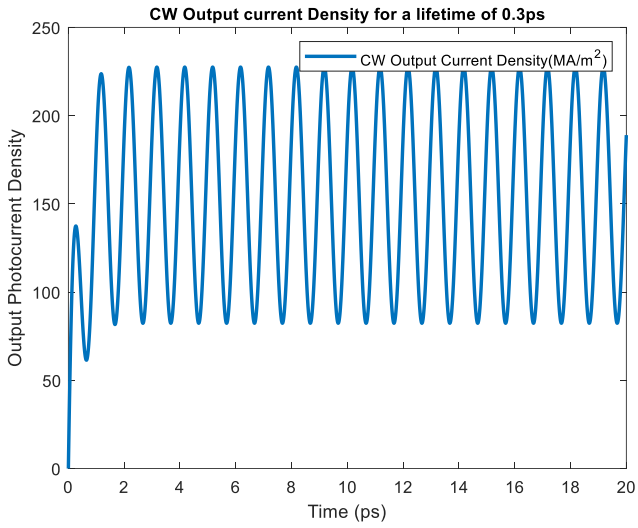


**Figure 2-8 CW Photocurrent Density with properties in table 2-1**

For CW systems, the ratio of THz wave to input pulse is relative to $\frac{\sqrt{I_1 I_2}}{I_1 I_2}$, and this factor would be maximized for $I_1 = I_2$. This condition is considered in Figure 2-7. Since the factor of $\frac{1}{\sqrt{1+\omega_{THz}^2 \tau_r^2}}$ is in the amplitude of CW THz generated photocurrent and wave, the bandwidth would be $\omega_{THz} = \frac{1}{\tau_r}$. The amplitude of current density for CW systems would be in the same order as the pulsed system,

thus the output current is in the range of $\mu A - nA$, but the radiated far-field in pulsed systems have a larger amplitude because of its dependence to $\frac{\partial J}{\partial t}$ which is larger in pulsed systems.

As discussed above, all the dimensions of volume in which the current moving, length of electrodes ($l$), the gap between electrodes ($g$), and depth of carrier penetration ($d$) are in the order of $\mu m$, which is much smaller than the wavelength of THz waves ($l, g, d \ll \lambda_{THz}$). By this assumption, a dipole model shown in Figure 2-9 for the generated current, is reasonable.

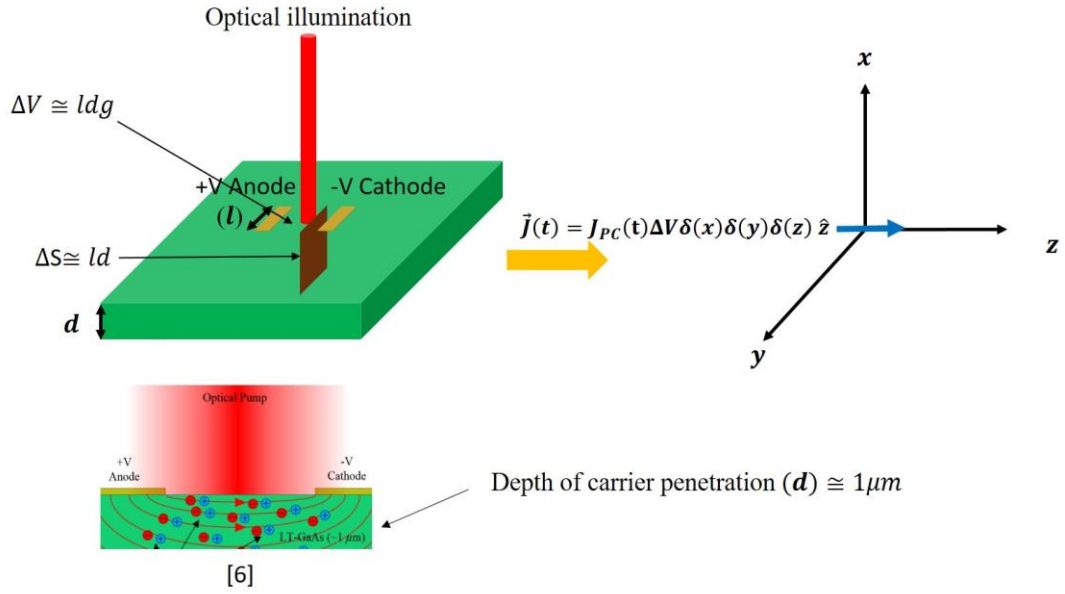


**Figure 2-9 Final model for THz photocurrent**

As shown in Figure 2-9, the cross-section the of current density's movement is $\Delta S = ld$, the gap between electrodes is $g$, so the volume of current's movement is $\Delta V = ldg$, and the calculated current has no spatial variation. Hence, by assuming the z-axis along with the current density, both CW and pulsed photocurrent are approximated as dipoles along the z-axis shown.

$$\vec{J}_{PC}(t) = J_{PC}(t)\Delta V\delta(x)\delta(y)\delta(z)\hat{z} \quad (2.22)$$

In (2.22), $J_{PC}$ is calculated in (2.14) and (2.15) for pulsed and CW photocurrent. The properties of near-field and far-field electric field of a dipole is discussed in appendix A.

## 2.4 Conclusion

In this chapter, after a short review of the methods of THz generation, the phenomena of photoconductivity for terahertz generation have been discussed and, by analyzing the properties of generated photocurrent, we have developed a simple dipole for the output photocurrent. For on-chip THz systems, the generated CW THz photocurrent has the potential to be used as the source, and the structure of the rest of this thesis is based on this assumption. In Chapter 4, dipoles are used to excite modes of the THz nanobeam cavity.

# Chapter 3
# Terahertz Waveguide Structures

This chapter reviews THz waveguide structures, but the main focus is on dielectric waveguides used in THz technology because of their potential to be used in integrated systems. A suspended silicon waveguide for 1 THz is simulated and analyzed in detail. This waveguide is also used in the nanobeam cavity analyzed in the next chapter.

## 3.1 Introduction

Waveguides are among the main building blocks for many different THz systems. Integrated electronics and photonics systems need low-loss waveguides to transmit electromagnetic waves between passive and active components, and for transitions from off-chip to on-chip. Waveguide structures for the THz frequency range are classified into two basic groups: metallic and dielectric waveguides.

For metallic waveguides, the developed technology for microwave and millimeter-wave range ($f < 300$ GHz) is extended to higher frequencies. This approach has two main challenges. First, higher fabrication precision is required, as the wavelength is orders of magnitudes shorter for THz compared to microwave and millimeter-wave. Second, the waveguide loss increases at higher frequencies, as this approach is based on metals, and the loss of metals increases at THz.

For dielectric waveguides, the developed technology for the optical frequencies is scaled up for the THz range. The operational principles of these waveguides are similar to those for optical waveguides, but the waveguide stack-ups and fabrication processes have unique challenges for these waveguide structures, especially at frequencies above 500 GHz [23,24].

### 3.1.1 THz Metallic Waveguides

Metallic waveguides are commonly used in microwave and millimeter-wave ranges. Using metals as boundaries in rectangular waveguides confines the electromagnetic field inside the structure. The same design of microwave rectangular metallic waveguides is scaled with smaller dimensions to work in the THz range.

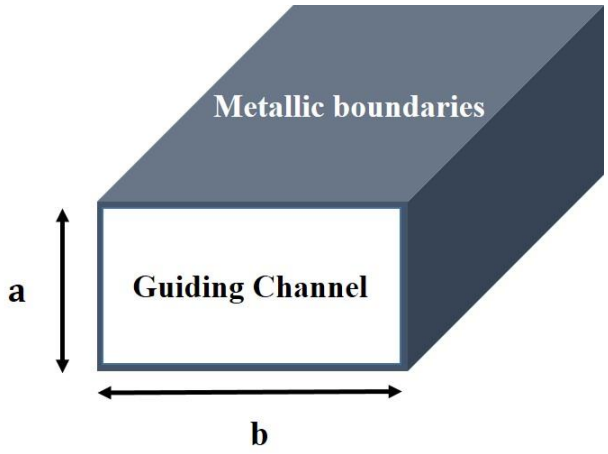


**Figure 3-1 Structure of rectangular metallic waveguides**

As shown in Figure 3-1, rectangular metallic waveguides are guiding channels surrounded by metals boundaries. The electromagnetic wave is confined inside the guiding channel due to the reflectivity of the metal. Since the transverse electric field in the metal boundaries is zero, the electric field outside the waveguide is zero. By solving the Helmholtz equation in these structures, an infinite number of discrete modes is calculated. Each mode of the waveguide has a propagation constant and cut-off frequency, and under the cut-off frequency, the wave cannot propagate inside the waveguide. The cut off frequency and the wave number of the waveguide mode designated by (m,n) can be found as:

$$f_{mn}^{c} = c\sqrt{\left(\frac{m}{2a}\right)^2 + \left(\frac{n}{2b}\right)^2} \quad , \quad \beta_{mn} = \frac{2\pi}{c}\sqrt{f^2 - {f_{mn}^{c}}^2} \qquad (3.1)$$

In (3.1), $f$ is the frequency of the electromagnetic wave, $mn$ is the index of each mode, $f_{mn}^{c}$ is the cut-off frequency, $\beta_{mn}$ is the propagation constant of $mn$'s mode, and $c$ is the speed of light. There are two problems in using these kinds of waveguides in the THz domain.

First, these waveguides have a high ohmic loss due to the finite conductivity of their metallic walls [25]. This loss is due to the surface resistance of metal at high frequencies discussed in [26].

$$R_s = \sqrt{\frac{\omega\mu(\omega)}{2\sigma(\omega)}} \quad (3.2)$$

In (3.2), $\omega$ is the angular frequency of the electromagnetic wave, $\mu(\omega)$ is the permeability of metal, and $\sigma(\omega)$ is the conductivity of the metal.

The propagation loss of the dominant mode ($\alpha_c^{TE_{10}}$) is calculated from [26].

$$\alpha_c^{TE_{10}} = \frac{R_s}{a^3 b \beta^{TE_{10}} \mu_0 \omega}\left(2\pi^2 b + a^3\left(\frac{\omega}{c}\right)^2\right)\left[\frac{Np}{m}\right] \quad (3.3)$$

Due to (3.3), by scaling the lengths of the waveguide and propagation constant by the wavelength for higher frequencies, the amount of loss per wavelength is approximately relative to $R_s$. In this case, $R_s$ increases because of the increment of frequency and also the decrement of a metal's conductivity. The conductivity is decreased due to the Drude-Lorentz model for conductivity [27].

$$\sigma = \frac{\sigma_0}{1 + j\omega\tau} \quad (3.4)$$

In (3.4), $\sigma_0$ is the low-frequency conductivity and $\tau$ is the mean free time of the electrons in metals, also called the relaxation time of electrons in metals. Due to the increment of $R_s$, the loss of metal per wavelength increases with an increase in frequency. This claim has been investigated in Table 3-1.

Second, the fabrication of these waveguides has a more complex process due to their lower dimensions. Also, the roughness of the metallic waveguides is a challenge because of the short wavelength of the THz waves, and the roughness needs to be much less than the wavelength.

Despite the challenges, metallic waveguides are fabricated and commercially used for frequencies up to 3THz [28]. Waveguides produced in [28], shown in Figure 3-2(a), have a propagation loss of between $0.18 - 0.28 \frac{\mathrm{dB}}{\mathrm{cm}}$ in WR-2.8 for 260-400 GHz, $0.47 - 0.67 \frac{\mathrm{dB}}{\mathrm{cm}}$ in WR-1.5 for 500-750 GHz, $0.88 - 1.3 \frac{\mathrm{dB}}{\mathrm{cm}}$ in WR-1.0 for 0.75-1.1 THz, and $4.3 - 6.3 \frac{\mathrm{dB}}{\mathrm{cm}}$ in WR-0.34 for 2.2-3.3 THz.

Since these commercial waveguides are bulky, they are not used in integrated systems. Using Deep Reactive Ion Etching (DRIE) on bulk silicon wafers can miniaturize these waveguides. The guiding channel is etched inside a silicon wafer by DRIE, and then surfaces of the channel are metalized by sputter coating.

Using DRIE in [29], a waveguide is fabricated for 350-460 GHz with an average propagation loss of $0.86 \frac{\mathrm{dB}}{\mathrm{cm}}$ and a deposited metal layer thickness of 7 μm.

In [30], [31], and [33], the micromachined waveguides are fabricated using DRIE for 325-440 GHz, 500-750 GHz, and 2.56-3.11 THz with an average propagation loss of $4 \frac{\mathrm{dB}}{\mathrm{cm}}$, $1.5 \frac{\mathrm{dB}}{\mathrm{cm}}$, and $13 \frac{\mathrm{dB}}{\mathrm{cm}}$ respectively.

Micromachined waveguides fabricated in [32] are WR-1 and have a sidewall roughness of 100 nm and propagation loss of $2 \frac{\mathrm{dB}}{\mathrm{cm}}$ for 0.75-1.1 THz. These micromachined designs still have ohmic losses, although the metal reflective layer is thin.

In Figure 3-2 the structures of waveguides micromachined using DRIE and the commercial waveguide are shown.

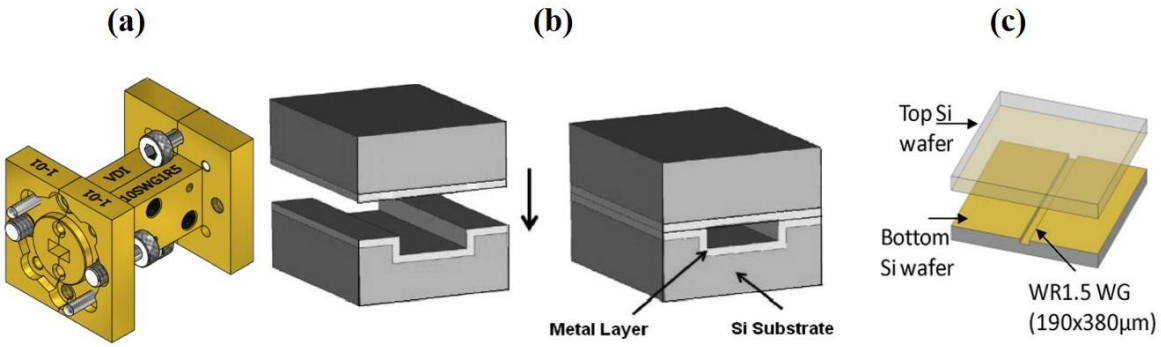


**Figure 3-2 (a) Schematic of commercial waveguides in [28] (b) Silicon-based rectangular waveguide with MEMS process [30] (c) Schematic drawing of WR1.5 Si micromachined waveguide [31]**

These structures and their properties are compared in Table 3-1.

| Waveguide structure | Frequency (THz) | Propagation loss (average) $\left(\frac{dB}{cm}\right)$ | Propagation loss (average) $\left(\frac{dB}{\lambda_0}\right)$ |
|---|---|---|---|
| VDI WR-2.8 [28] | 0.26-0.4 | 0.23 | 0.021 |
| VDI WR-1.5 [28] | 0.5-0.75 | 0.57 | 0.027 |
| VDI WR-1.0 [28] | 0.75-1.1 | 1.09 | 0.035 |
| VDI WR-0.34 [28] | 2.2-3.3 | 5.3 | 0.058 |
| Micromachined waveguide [29] | 0.35-0.46 | 0.86 | 0.064 |
| Micromachined waveguide [30] | 0.325-0.44 | 4 | 0.314 |
| Micromachined WR-1.5 [31] | 0.5-0.75 | 1.5 | 0.072 |
| Micromachined WR-1.0 [32] | 0.75-1.1 | 2 | 0.065 |
| Micromachined waveguide [33] | 2.56-3.11 | 13 | 0.138 |

**Table 3-1 Comparison of different metallic waveguide structures**

### 3.1.2 THz Dielectric Waveguides

Dielectric waveguides are widely used in optical systems. Rather than the metallic reflectivity in metallic waveguides, dielectric ones are based on total internal reflection between two dielectric materials with different refractive indices. The theoretical and numerical investigation of dielectric waveguides for the THz region was researched in the 1990s for the first time [34,35]. The absence of conduction loss is the main advantage of these waveguides. Also, for higher frequencies, roughness of materials is an important issue and must be much less than the wavelength of electromagnetic waves. The fabrication of dielectric waveguides is more appropriate than that of metallic ones due to this respect. The propagation losses for these waveguides are caused by material absorption and the radiative loss.

Materials with a large refractive index and low absorption loss are crucial for high modal confinement. Due to the very low absorption coefficient and large non-dispersive refractive index in the TH region, high-resistivity silicon (HR-Si) is used for guiding the channel of THz dielectric waveguides.

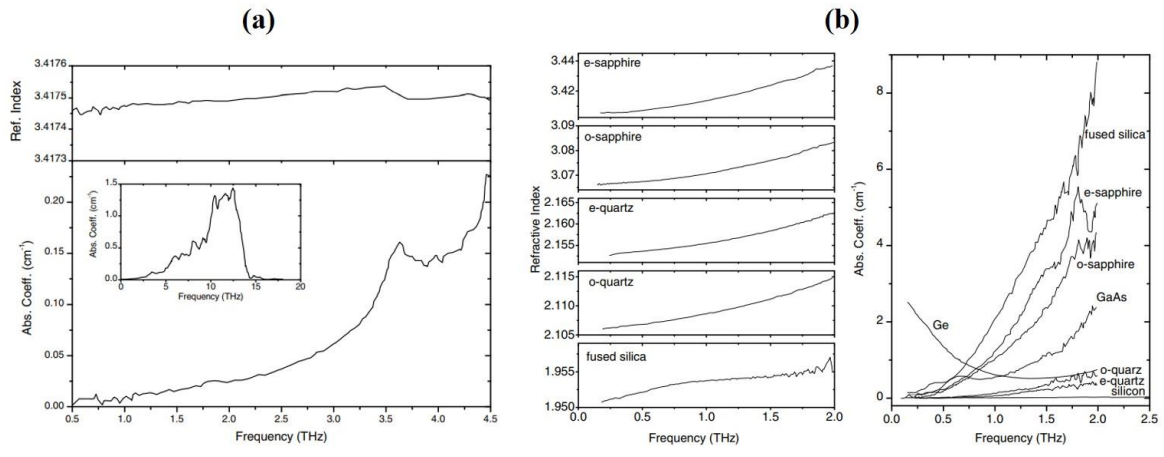


**Figure 3-3 (a) Refractive index and absorption coefficient of HR-Si (b) Refractive index and absorption coefficient of sapphire, quartz, and fused silica in the spectral range 0.2-2 THz [10]**

As shown in Figure 3-3, HR-Si has the most transparency and least refractive index dispersion in the range of THz. Its absorption coefficient is less than $0.02\,\frac{1}{\mathrm{cm}}$, and the variation of its refractive index is less than $10^{-4}$ below 1THz.

The realization of THz dielectric waveguides has been investigated very recently. A suspended HR-Si waveguide with holding arms has been developed for 90-220 GHz with a loss of less than $0.087\,\frac{\mathrm{dB}}{\mathrm{cm}}$ [36], shown in Figure 3-4(a), and the same method is used for higher frequencies, 100-200 GHz in [37] and 500-750 GHz in [38] with an average loss of $0.65\,\frac{\mathrm{dB}}{\mathrm{cm}}$.

Another method, reported in [39] and shown in Figure 3-4(b), is based on silicon on glass (SOG) technology using pyrex as the substrate for HR-Si, with losses of $0.63\,\frac{\mathrm{dB}}{\mathrm{cm}}$, $0.28\,\frac{\mathrm{dB}}{\mathrm{cm}}$, and $0.53\,\frac{\mathrm{dB}}{\mathrm{cm}}$ for 55-65 GHz, 90-110 GHz, and 140-170 GHz respectively. For frequencies beyond 200 GHz, the loss of pyrex increases; hence, to avoid this material loss, etching of the pyrex underneath the guiding channel is proposed in [40] and shown in Figure 3-4(c) for 440-500 GHz with an average loss of $0.54\,\frac{\mathrm{dB}}{\mathrm{cm}}$. The guiding channel in Figure 3-4 (c) is suspended by silicon supporting beams similar to those in Figure 3-4(a). This waveguide has been extended in frequency for 420-590 GHz in [47].

Another silicon on glass (SOG) waveguide using quartz as the substrate for HR-Si has been developed for 500-580 GHz with a loss of $0.46\,\frac{\mathrm{dB}}{\mathrm{cm}}$, as shown in Figure 3-4(d) [23].

A U-shaped SOG waveguide (U-SOG) operating at very high frequencies of 0.9-1.08 THz proposed in [41], has an average loss of $1.9\,\frac{\mathrm{dB}}{\mathrm{cm}}$ (Figure 3-4(e)). The field of the dominant mode is confined in the upper side of the HR-Si channel, and to prevent the loss of pyrex substrate at high frequencies, a layer is etched between the silicon and pyrex.

There are other types of dielectric waveguides based on photonic crystal structures. The waveguide reported in [42] and shown in Figure 3-4(f) was designed for 540-630 GHz and has an average loss of $4\frac{\mathrm{dB}}{\mathrm{cm}}$. This waveguide uses the refractive index contrast between air/HR-Si and glass/HR-Si for the top and bottom and uses the bandgap properties of a photonic crystal in the y-axis for guiding. Again to reduce the loss of pyrex, a layer is etched under the HR-Si guiding channel. Periodic holes are etched in the HR-Si on both sides of the guiding channel to create a bandgap in which the field is prohibited to propagate, and the field is confined inside the HR-Si guiding channel. Photonic crystals and their properties and applications will be discussed in the next chapter. The high loss of this waveguide is mainly the result of the large number of etched holes, which greatly increase the scattering losses. To reduce the scattering loss in photonic crystal structures, the main method is tapering the holes, and this has been discussed in the next chapter.

Another fully suspended line defect photonic crystal waveguide design shown in Figure 3-4(g) with lower propagation losses was presented in [43]. The disadvantage of this design is that the very low measured propagation loss of $0.1\frac{\mathrm{dB}}{\mathrm{cm}}$ covers only a very short frequency band region of 326-331 GHz.

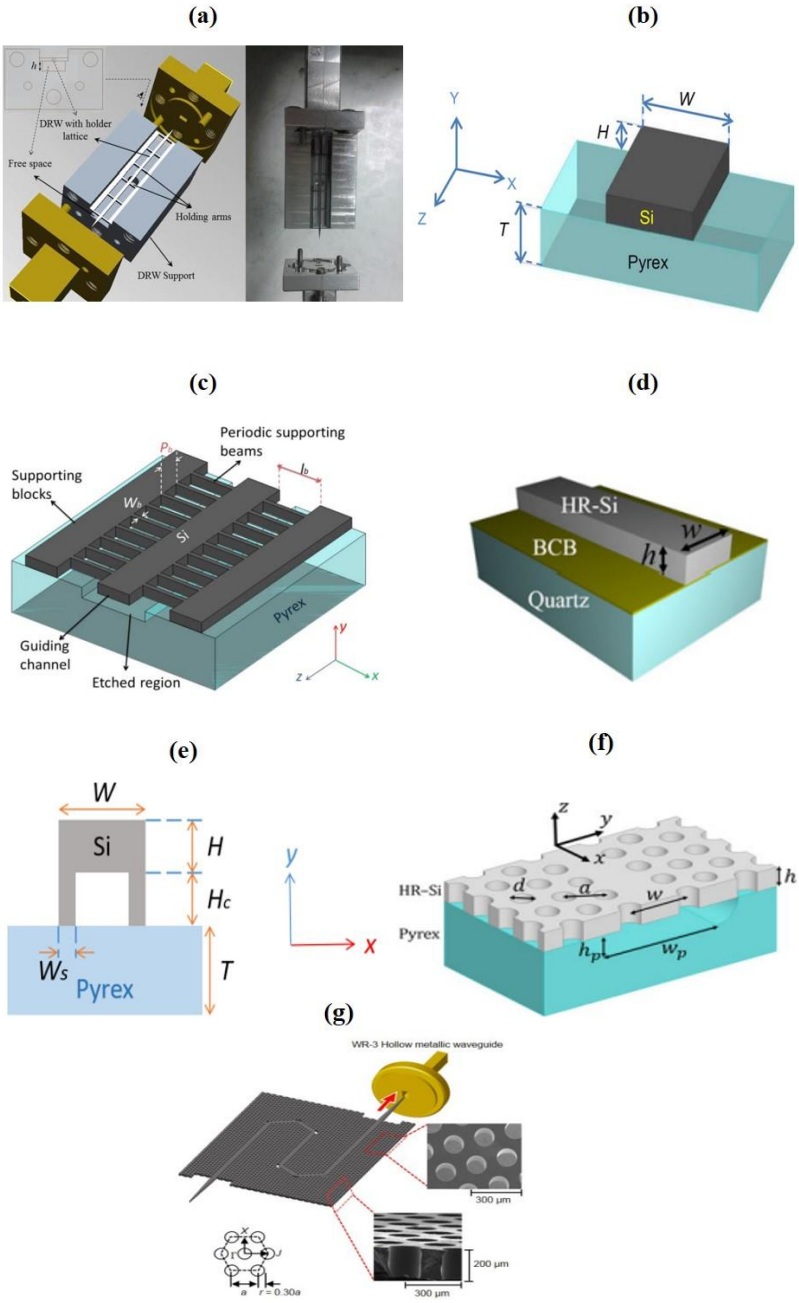


**Figure 3-4 Dielectric waveguide structures for the frequency range of (a) 90-140 GHz [36] (b) 55-170 GHz [39] (c) 440-500 GHz [40] (d) 500-580 GHz [23] (e) 0.9-1.08 THz [41] (f) 500-700 GHz [42] (g) 326-331 GHz [43]**

Different THz dielectric waveguide structures and their properties are compared in Table 3-2.

| Waveguide structure | Frequency (THz) | Propagation loss (average) $\left(\frac{dB}{cm}\right)$ | Propagation loss (average) $\left(\frac{dB}{\lambda_0}\right)$ |
|---|---|---|---|
| Suspended HR-Si [36] | 0.09-0.22 | 0.087 | 0.02 |
| HR-Si on pyrex [39] | 0.14-0.17 | 0.53 | 0.1 |
| Suspended line-defect photonic crystal [43] | 0.326-0.331 | 0.1 | 0.009 |
| Suspended HR-Si on pyrex [40] | 0.44-0.5 | 0.54 | 0.0346 |
| HR-Si on quartz [23] | 0.5-0.58 | 0.46 | 0.026 |
| Line defect photonic crystal [42] | 0.54-0.63 | 4 | 0.208 |
| Suspended HR-Si [38] | 0.5-0.75 | 0.65 | 0.032 |
| U-SOG [41] | 0.9-1.08 | 1.9 | 0.059 |

**Table 3-2 Comparison of different dielectric waveguide structures**

As shown in Tables 3-1 and 3-2, HR-Si suspended structures have the lowest loss because of the low material loss of HR-Si and the lack of ohmic loss. In addition, these structures are compatible with integrated systems that are also based on silicon. Hence, the choice for the remaining part of this thesis is a suspended HR-Si waveguide designed for 1 THz. The design flow and properties of the waveguide will be discussed in the next section (3.2). This suspended HR-Si waveguide is used to design a nanobeam cavity in Chapter 4.

## 3.2 Analysis of a Silicon Dielectric Waveguide for 1THz

As discussed above, one potentially beneficial solution for a waveguide to use in an integrated system is a dielectric waveguide with a suspended HR-Si guiding channel, so we next analyze a suspended HR-Si waveguide for 1 THz. The structure of the waveguide is shown in Figure 3-5.

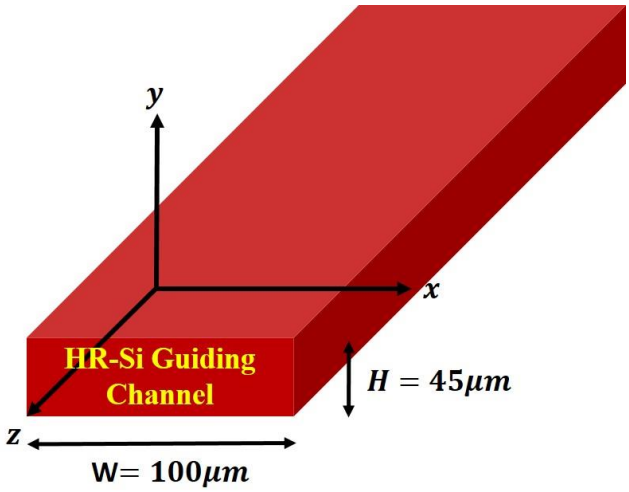


**Figure 3-5 Geometrical structure of analyzed waveguide**

To find the dimensions of the waveguide in Figure 3-5, we consider two important factors: 1) the waveguide must be single-mode near 1 THz ($\lambda_0 = 300\mu m$) and have a good field confinement for the first mode, and 2) it must have the capability to design a high quality factor nanobeam cavity inside it, which will be discussed in the next chapter. The dimensions to satisfy both conditions are found by $W = 100\mu m = \frac{\lambda_0}{3}$ for the width of the waveguide and $H = 45\mu m = \frac{\lambda_0}{6.67}$ for the height of the waveguide. These numbers are comparable with the U-SOG waveguide in [41], which was discussed in 3.1.2, and have been investigated by running different simulations for the waveguide and the nanobeam introduced in the next chapter. Since the field is propagating along the z-axis, it is assumed to be infinite along z.

Because of the special properties of HR-Si in the THz region, the guiding channel is made from HR-Si with the refractive index of $n_{HR-Si} = 3.4174$ and three-dimensional conductivity of $\sigma_{HR-Si} = 0.01 \frac{S}{m}$ found in [24] and [44].

In the modal analysis of waveguides, we are studying to find the solutions of the Helmholtz equation with a flow of energy along the guiding channel and not

perpendicular to it. Consequently, the fields will be appreciable only in the immediate neighborhood of the guiding structures. The electric field and the magnetic field of guided modes at an angular frequency of $\omega$ in waveguide structures that have constant cross-section and infinite length are represented in equations (3.5) and (3.6).

$$\vec{E}^m(\vec{r},\omega) = \vec{e}^m(x,y,\omega)e^{-\alpha^m(\omega)z}e^{-j\beta^m(\omega)z} \quad (3.5)$$

$$\vec{H}^m(\vec{r},\omega) = \vec{h}^m(x,y,\omega)e^{-\alpha^m(\omega)z}e^{-j\beta^m(\omega)z} \quad (3.6)$$

In (3.5) and (3.6), $\beta^m(\omega)$ is the propagation constant, $\alpha^m(\omega)$ is the propagation loss, $\vec{e}^m(x,y,\omega)$ is the electric field, and $\vec{h}^m(x,y,\omega)$ is the magnetic field for mode $m$ at the angular frequency of $\omega$. We need to find $\beta(\omega)$, $\alpha(\omega)$, $\vec{e}^m(x,y,\omega)$, and $\vec{h}^m(x,y,\omega)$ for each propagating mode of the waveguide.

In dielectric planar waveguides like slabs, the solutions are calculated analytically, but there exists no analytical solution for three-dimensional open channel waveguide modes (except for the modes of the round step-index fiber) in the closed-form [45]. Modes of three-dimensional waveguides with widths larger than their thickness, and waveguiding across the width that is not stronger than the waveguiding across their thickness can be calculated approximately by the effective index method described in [46].

In addition, in planar dielectric waveguides, there are TE and TM modes, meaning that there are modes with $e_z = 0$ for TE modes and modes with $h_z = 0$ for TM modes, but in three-dimensional dielectric waveguides, the modes are hybrid meaning that all the modes have electric and magnetic fields along the z-axis. For waveguide channels with a higher width than thickness, a mode with its electric field mostly in the x-direction parallel to the planar layers is called a TE-like mode, and one with its magnetic field mostly in this direction is called a TM-like mode [46].

To analyze this waveguide, we use both Lumerical FDE and HFSS solvers to ensure the accuracy od solutions for the properties of each propagating mode of the waveguide. The structures simulated with the two solvers are shown in Figure 3-6.

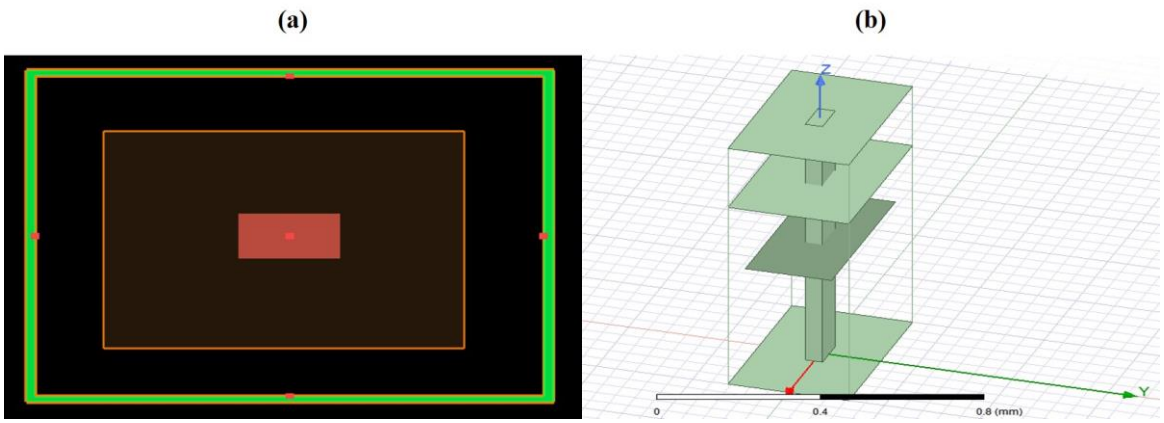


**Figure 3-6 (a) Simulation area in Lumerical FDE (b) Simulation Volume in HFSS**

As shown in Figure 3-6 (a), in the Lumerical FDE solver, using finite difference eigenmode in the transverse cross-section of the waveguide (two-dimensional analysis) solves the Helmholtz equation to find the mode profiles, effective index, and loss of modes of the waveguide. The effective index of mode m is $n_{eff}^{m}(\omega) = \frac{\beta^{m}(\omega)c}{\omega}$ which is $1 < n_{eff}^{m}(\omega) < n_{HR-Si}$ for the guided modes of waveguide. The loss of mode m is equal to $loss^{m}(\omega) = 8.686\alpha^{m}(\omega)\ [\frac{dB}{m}]$. The boundaries of the simulation are assumed to be metals with dimensions $5W$ along the x-axis and $7H$ along the y-axis because the fields of the waveguide modes are zero near these boundaries. Using PMLs as the simulation boundaries are is another solution, but it increases the time of simulation dramatically. The $1\mu m$ mesh sizes near the waveguide are assumed to be more accurate.

For HFSS simulation, as shown in Figure 3-6(b), Maxwell's equations are solved in a three-dimensional volume with the same size of Lumerical FDE simulation in the x-y plane and a length of $l = 3\lambda_0 = 900\mu m$ to find the properties of waveguide

modes. The simulation volume boundaries are assumed to be radiation boundary conditions to prevent reflections from the simulation area boundaries. Two wave ports at the ends of the structure in the x-y plane ($z = 0, z = l$) excite the waveguide modes inside the structure. In HFSS, wave ports are excitation sources at the boundaries of the structure that solve the Helmholtz equation in the cross-section of the waveguide and then inject the field of each modes into the structure.

After the simulation is run, we must determine $n_{eff}^{m}(\omega)$ and $loss^{m}(\omega)$ for each mode of the waveguide as a function of frequency and the amplitude of the electric field and magnetic field ($|\vec{e}^{m}(x,y,\omega)|, |\vec{h}^{m}(x,y,\omega)|$) of each mode at the frequency of 1 THz.

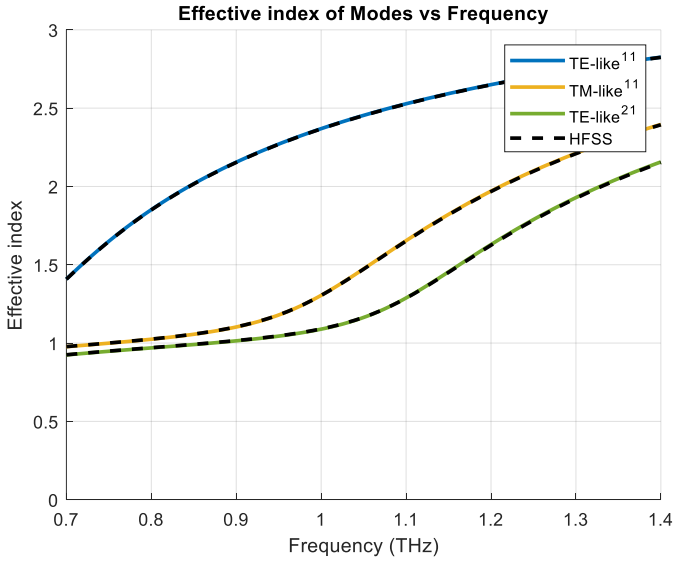


**Figure 3-7 Effective index of waveguide modes in Lumerical FDE and HFSS for the frequency range of 0.7-1.4**

As shown in Figure 3-7, there are three propagating modes in the frequency range of 0.7-1.4 THz. Our naming convections for these modes are discussed in this section. Since the first mode has a much higher effective index at 1 THz, and also because its field is confined much better than the others as will be shown later, this waveguide is approximately single mode. In addition, the results in HFSS and

Lumerical FDE are completely the same, which we take as confirmation that these solutions are right for the effective index of waveguide modes as a function of frequency.

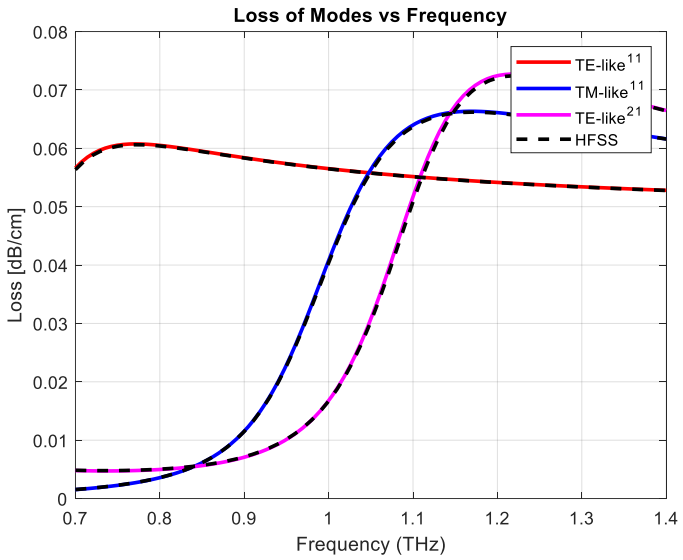


**Figure 3-8 loss of waveguide modes in Lumerical FDE and HFSS for the frequency range of 0.7-1.4 THz**

As shown in Figure 3-8, the loss of the first mode of the waveguide at 1 THz is approximately $\text{loss} = 0.057\,\frac{\text{dB}}{\text{cm}}$, which is quite low. Again, the solutions in HFSS and Lumerical FDE are the same, confirming their accuracy.

As shown in figure 3-9 (a), the electric field is confined inside the guiding channel very well for the first mode, but it is not confined well for the other modes.

As shown in Figures 3-9(a) and 3-9(b), for the first mode of the waveguide, the electric field is mostly along the x-axis, and it has one peak relative to width and one peak relative to thickness; thus, this mode is a $\text{TE}-\text{like}^{11}$ mode. For the second mode of the waveguide, the magnetic field is mostly along the x-axis, and it has one peak relative to width and one peak relative to thickness; thus, this mode is a $\text{TM}-\text{like}^{11}$ mode. For the third mode of the waveguide, the electric field is

mostly along the x-axis, and it has two peaks relative to width and one peak relative to thickness; thus, this mode is a $TM-like^{21}$ mode. Hence, based on these findings, the modes of the waveguide have been defined, and their properties have been investigated and are shown in Figures 3-7 to 3-10.

**(a)**

| | Amplitude of electric field in HFSS $\lvert\vec{e}^{m}(x, y, 1\ THz)\rvert$ | Amplitude of magnetic field in HFSS $\lvert\vec{h}^{m}(x, y, 1\ THz)\rvert$ |
|---|---|---|
| Mode $TE-like^{11}$ | 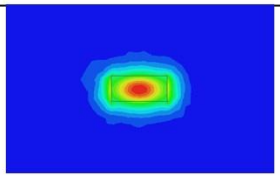 | 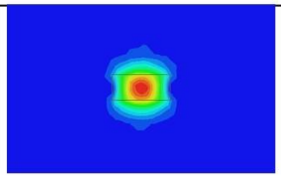 |
| Mode $TM-like^{11}$ | 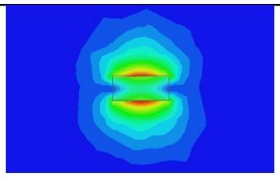 | 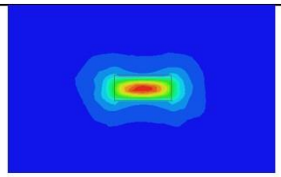 |
| Mode $TE-like^{21}$ | 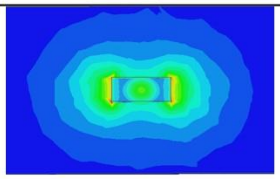 | 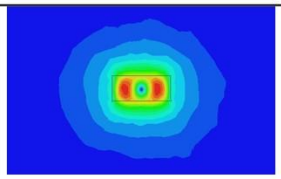 |

**(b)**

| Amplitude of electric field along x-axis for Mode $TE-like^{11}$ in Lumerical FDE $\lvert\vec{e}_x^{TE-like^{11}}(x, y, 1\ THz)\rvert$ | Amplitude of magnetic field along x-axis for Mode $TM-like^{11}$ in Lumerical FDE $\lvert\vec{h}_x^{TM-like^{11}}(x, y, 1\ THz)\rvert$ | Amplitude of electric field along x-axis for Mode $TE-like^{21}$ in Lumerical FDE $\lvert\vec{e}_x^{TE-like^{21}}(x, y, 1\ THz)\rvert$ |
|---|---|---|
| 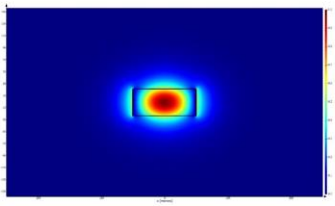 | 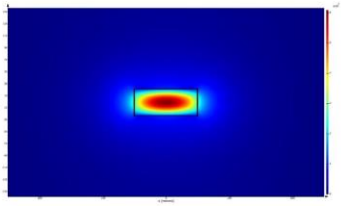 | 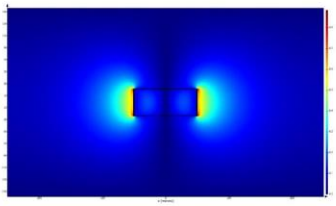 |

**Figure 3-9 (a) Amplitude of electric and magnetic field of each mode in HFSS (b) Amplitude of electric or magnetic field along the x-axis in Lumericl FDE to determine the TE-like and TM-like modes and their indices**

Finally, it is important to know about the electric field vector of each mode for the excitation of the waveguide. As shown in Figure 3-10, only the $TE-like^{11}$

mode has a strong electric field along the x-axis at the center of the waveguide relative to the y-axis; thus, by an excitation like that shown in Figures 1-1 and 2-9, only the first mode will excite and propagate inside the waveguide structure.

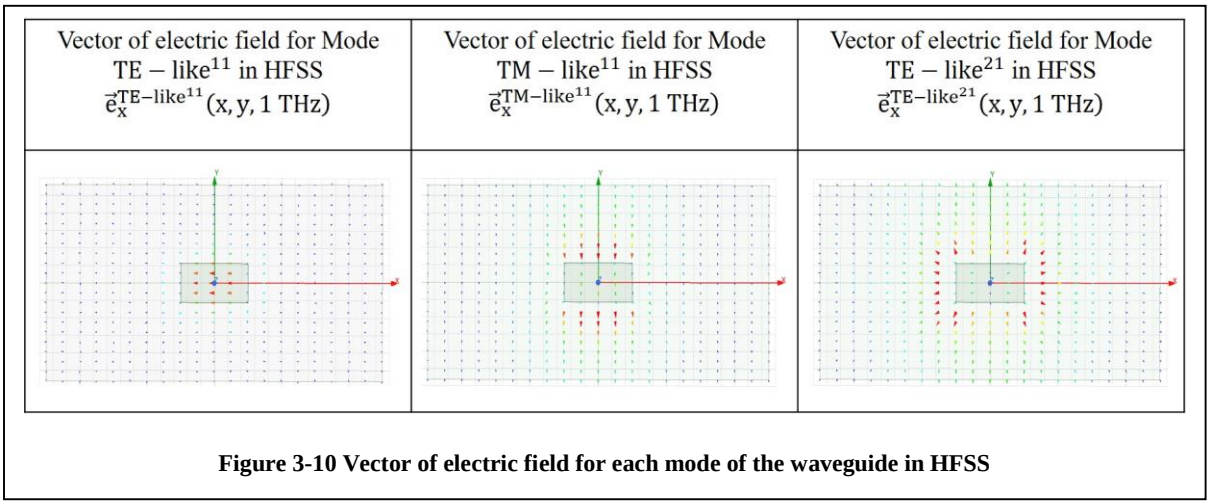


**Figure 3-10 Vector of electric field for each mode of the waveguide in HFSS**

## 3.3 Conclusion

In this chapter, different technologies for THz waveguides have been reviewed to find an appropriate structure for an integrated THz system. A suspended HR-Si waveguide channel with the size of $45\mu m \times 100\mu m$ has been simulated and analyzed. The designed waveguide has a loss of $0.057\frac{dB}{cm}$ at 1 THz and is approximately $TE-like^{11}$ single mode with an electric field mostly along the x-axis, appropriate for connection to the CW photoconductive THz source of Figures 1-1 and 2-9. The nanobeam cavity of the next chapter (Chapter 4) is based on this waveguide.

# Chapter 4

# Terahertz Photonic Crystal Nanobeam Cavity

This chapter examines a photonic crystal nanobeam cavity in the THz region. In the previous chapter, a suspended silicon waveguide was analyzed, and this chapter's goal is to design a photonic crystal nanobeam cavity (PCNC) inside that waveguide. The size of the waveguide is chosen by scaling different optical structures to achieve a high quality factor nanobeam cavity inside the waveguide. After a review of photonic crystals with a focus on PCNCs, a PCNC for 1 THz is designed and analyzed.

## 4.1 Introduction

In optics, ultra-high quality factor (Q) resonators enhance the probability of interaction between light and matter because of their ability to store photons for many optical cycles. They are thus used in applications ranging from optoelectronics and nonlinear optics to biomechanical sensing, cavity quantum electrodynamics, and optomechanics [48]. Cavities based on traveling waves such as whispering gallery structures, which include micro-toroid resonators, as well as micro-sphere resonators have been used to achieve some of the largest Q factors [49]. As shown in [49], a Q factor of $8 \times 10^9$ has been reported in a micro-sphere cavity, but if the figure of merit is related to the ratio between the Q factor of the resonator and mode volume ($\frac{Q}{V_{mode}}$), standing wave resonators capable of having a very small mode volume have been reported as an alternative solution [49]. Three-dimensional photonic crystal structures were the starting point for finding an appropriate structure for a standing wave resonator with a high $\frac{Q}{V_{mode}}$ based on Fabry-Perot geometry. This geometry consists of a region for the propagation of light and terminates at both sides with optical mirrors in photonic crystals. Because of the challenges in the fabrication of three-dimensional structures, efforts

continued to find an appropriate structure in one-dimensional photonic crystals with an easier fabrication process [48]. Photonic crystal nanobeam cavities (PCNCs) have been identified as one of the best solutions since they have a high $\frac{Q}{V_{mode}}$ and can be easily integrated with optical waveguides for efficient light coupling. To understand how PCNCs work, first, photonic crystals are briefly reviewed, followed by an explanation of PCNCs.

## 4.2 Photonic Crystals

Photonic crystals are designed as periodic structures to control the propagation of electromagnetic waves. The functionality of photonic crystals is similar to that of solid-state crystals, which are used to control the propagation of electrons naturally by means of their bandgaps of energy in which electrons cannot propagate. In photonic crystals, electromagnetic waves are also unable to propagate in bandgaps of frequency, and by engineering these structures, applications such as waveguides, metamaterials, resonators, and many others can be designed. In 1987, the first study between solid crystals and three-dimensional refractive index structures was done in [50], and in 1989 the first three-dimensional photonic crystal structure with a complete bandgap was designed in [51]. Photonic crystals can be designed as one, two, or three-dimensional structures as shown in Figure 4-1.

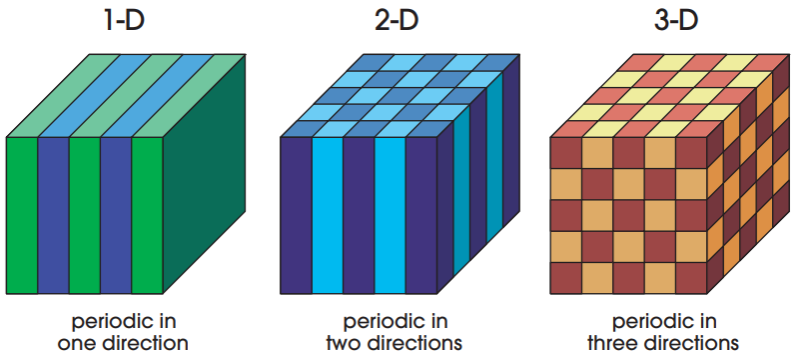


**Figure 4-1 Simple examples of one-, two-, and three-dimensional photonic crystals. The different colors represent materials with different refractive indices. [52]**

### 4.2.1 Photonic Crystal Nanobeam Cavities

Photonic crystal nanobeam cavities are one-dimensional waveguide-based periodic structures. Waveguide-based micro-cavities were designed for the first time in 1997 [53]. As shown in figure 4-2, the structure consists of a cavity inside the waveguide surrounded with two lattices of holes that play the role of Bragg mirrors. This structure is designed for a resonance wavelength of $\lambda = 1.54\,\mu m$. In this cavity, light is trapped by a combination of Bragg scattering in the longitudinal direction and total internal reflection in two transverse directions, and the quality factor of this structure is 265.

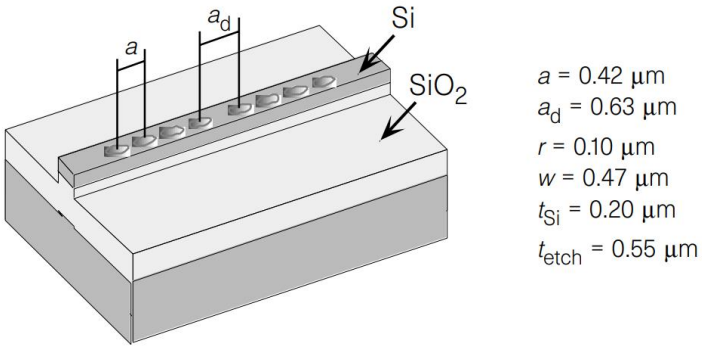


**Figure 4-2 Schematic of photonic crystal nanobeam cavity [53]**

The low value of the quality factor occurs because of the light scattering at the interface of the Bragg mirrors and the central cavity, as shown in Figure 4-3(a), because of the mismatch in the effective mode indices of the two regions [48]. This scattering can be decreased by tapering the holes as shown in Figure 4-3(b). The cavity can be considered as a Fabry-Perot cavity, which traps the nanobeam waveguide mode. Since the cavity mode penetrates some distance into the mirrors, it is crucial that the fields do not abruptly terminate at the mirror boundaries as doing so would cause considerable scattering loss. Tapering the propagating mode of the cavity region into the exponentially decaying mode of the Bragg mirrors is

the solution to increasing the quality factor of nanobeam cavities. Hence, the waveguide mode index is reduced slowly to match the Bragg mirror index causing a significant reduction of scattering and providing an increase of the quality factor [54].

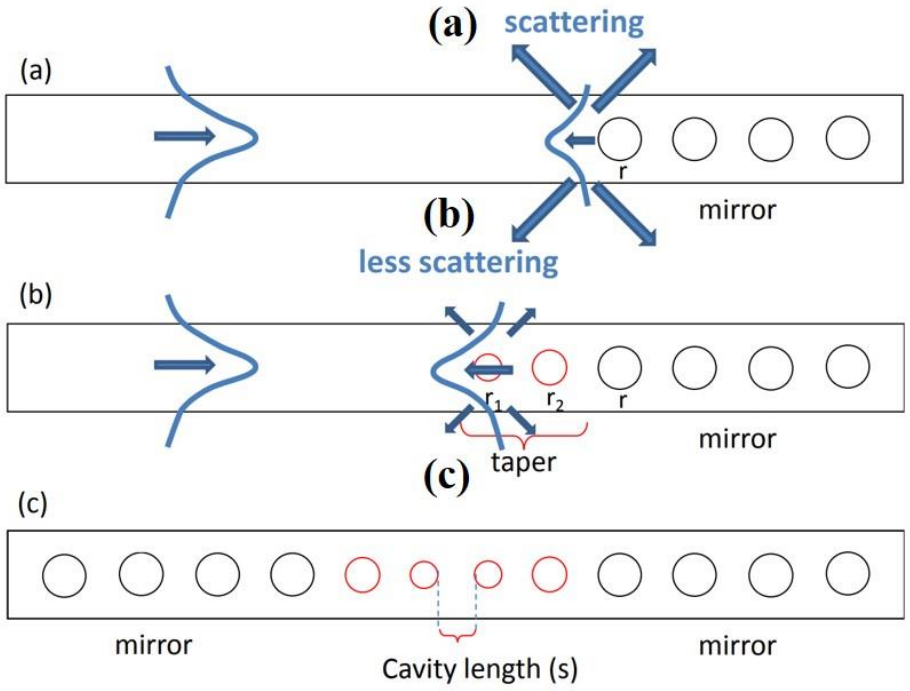


**Figure 4-3 (a) light scattering at waveguide- mirror interface (b) schematic showing the reduced scattering loss due to tapering (c) photonic crystal nanobeam cavity formed by using two tapered mirrors [54]**

As shown in Figure 4-4, PCNCs consist of three parts: first, the cavity length, which is sandwiched between two periodic Bragg mirrors; second, the tapered holes, which reduce the scattering of cavity modes inside the Bragg mirrors region; and third, the Bragg mirrors, which reflect the light to trap it inside the cavity.

The range of the quality factor of these cavities varies with the change of material and when different tapering structures are used. As reported in [55], this range varies from 700 to the order of $10^7$. The tapering side is based on the excitation of the cavity. If the cavity is excited from the center as has been done in [56], the

tapering side is in the center of the cavity, but if the excitation is from the sides of the waveguide as in [38], the tapering is at the beginning and the end of Bragg mirrors.

In the THz region, nanobeam cavities have not been used much. In [37], a nanobeam cavity with Gaussian distribution for the tapering holes has been designed for 100 GHz with a quality factor of 11900. The material of this structure is HR-Si, and the excitation is from the sides of the waveguide; thus, the tapering holes are at the beginning and end of the periodic structure. In [38], another nanobeam cavity with parabolic distribution for the tapering holes has been designed for 650 GHz with a quality factor of 18000. The material and the excitation of this cavity are the same as those in [37].

Since a photonic crystal nanobeam cavity excited from the center of the cavity has not been designed in the THz region yet, in the next section, we undertake such a design based on existing optical design approaches.

### 4.3 Analysis of a Photonic Crystal Nanobeam Cavity for 1THz

In this work, the main reason for using a photonic crystal nanobeam cavity inside the waveguide is to trap the generated photocurrent THz wave to couple it to the waveguide. The structure of the cavity has been shown in Figure 4-4. If the quality factor of the cavity is high enough, the generated THz wave will be trapped inside the cavity and will be coupled to the waveguide by further design. Since the photoconductive source is assumed to be at the center of the structure, tapering holes have been designed at the center of the structure for mode matching between the cavity and Bragg mirrors.

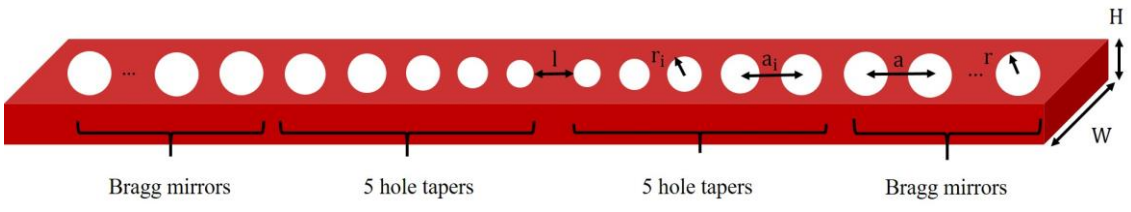


**Figure 4-4 Schematic of analyzed photonic crystal nanobeam cavity**

In Figure 4-4, l is the length of the cavity, $r_i$ is the radius of tapers, $a_i$ is the distance of tapers, r is the radius of Bragg mirror holes, H is the height of waveguide, and W is the width of the waveguide.

The idea of using 5 taper holes and the initial values of the properties of the nanobeam cavity have been studied in [56], but all the values have been optimized to design a cavity for 1 THz. Since the cavity is designed inside the waveguide of the previous chapter, the height and the width of the waveguide are the same as in the previous chapter, but other values of the structure have been reported in Table 4-1. The material of the structure is HR-Si, the same as that in the previous chapter and with the same properties. There are 7 holes as Bragg mirrors in this structure in each side.

| $a_1$ | $a_2$ | $a_3$ | $a_4$ | $a_5$ | $r_1$ | $r_2$ | $r_3$ | $r_4$ | $r_5$ | a | r | l |
|---|---|---|---|---|---|---|---|---|---|---|---|---|
| 63.46 | 67.31 | 71.15 | 75 | 78.85 | 17.77 | 18.85 | 19.92 | 21 | 22.08 | 82.96 | 23.23 | 27.55 |

**Table 4-1 Values of the properties of the structure (the unit of values is µm)**

For the simulation of this structure, the three-dimensional FDTD solver of Lumerical has been used. The simulation structure is shown in Figure 4-5.

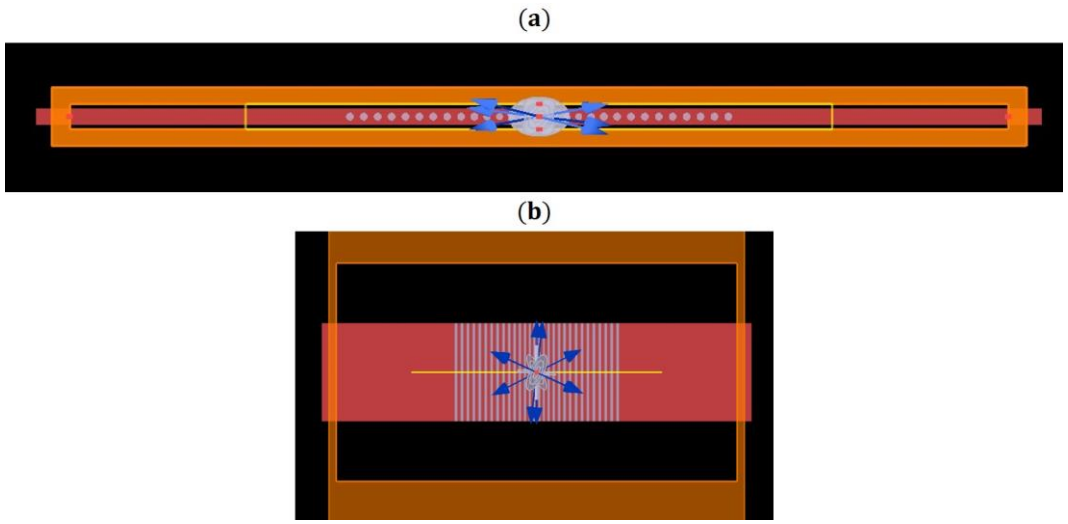


**Figure 4-5 Structure of Lumerical FDTD simulation in the (a) x-y plane (b) x-z plane**

In this simulation, the waveguide is expanded along the x-axis, its width is along the y-axis, and its height is along the z-axis. The simulation volume is 5600 µm along the x-axis, 150 µm along the y-axis, and 100 µm along the z-axis. All the boundary conditions are perfectly matched layers (PML) to avoid the reflections from the boundaries.

To excite the modes of the cavity, a dipole cloud at the center of the cavity containing 20 electric dipoles in the frequency range of 0.9-1.1 THz has been used to excite all the modes of the cavity. These dipoles are in different random directions that can excite all the modes of the cavity with fields along any direction. Since the cavity is designed for a particular mode with a field along the width of the cavity in 1 THz, only this mode will excite.

To obtain the quality factor of the cavity, a high Q analyzer has been used at the center of the cavity. Since the quality factor of this cavity is high, it takes a long time for the field to decay; thus, it takes a very long simulation time to calculate the quality factor from the decaying of the field. A high Q analyzer calculates the quality factor using the formula (4.1).

$$Q = -\frac{2\pi f_R \log_{10}(e)}{2m} \quad (4.1)$$

In (4.1), $f_R$ is resonance frequency and m is the slope of the decay of the field. This analyzer monitors the field inside the cavity over time, then calculates the spectrum of the field by a Fourier transform, and finds the quality factor by using (4.1).

To find the mode field of the cavity, a frequency domain field and power monitor have been used in the x-y plane. This monitor collects the field profile in the frequency domain from simulation results across some spatial regions within the simulation in the FDTD solver.

The simulation time is assumed to be 1ns, which is large enough to find the results of the simulation.

As shown in Figure 4-6, the spectrum of the field has two resonant modes: at 937 GHz and 1 THz. We are looking to find out the properties of the 1 THz mode of the cavity. The quality factor of the resonance mode at 1 THz was found to be 1023. This quality factor is large enough to trap the generated THz wave for coupling to the waveguide.

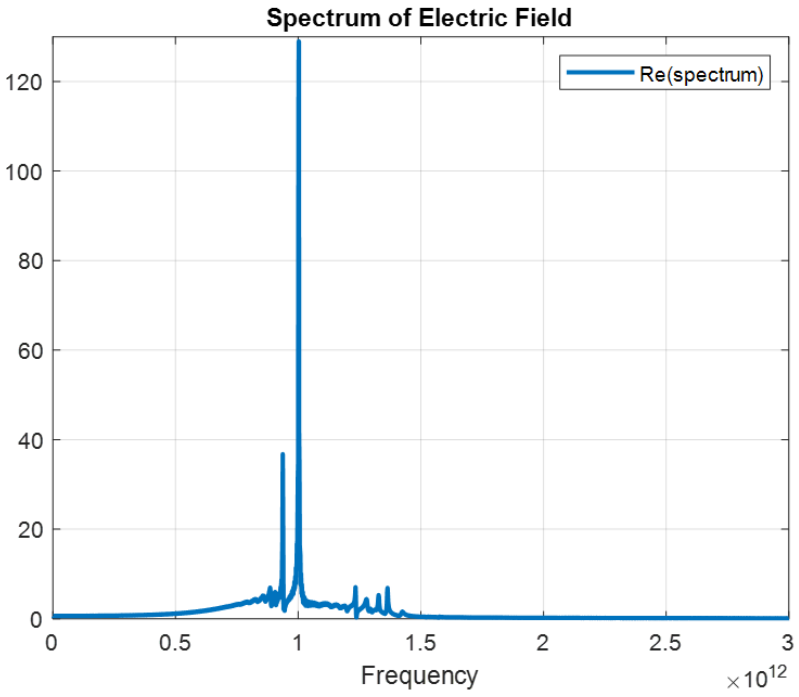


**Figure 4-7 Spectrum of Electric field of high Q analyzer in Lumerical**

The field profile of the 1 THz resonance mode has been shown in Figures 4-8 and 4-9.

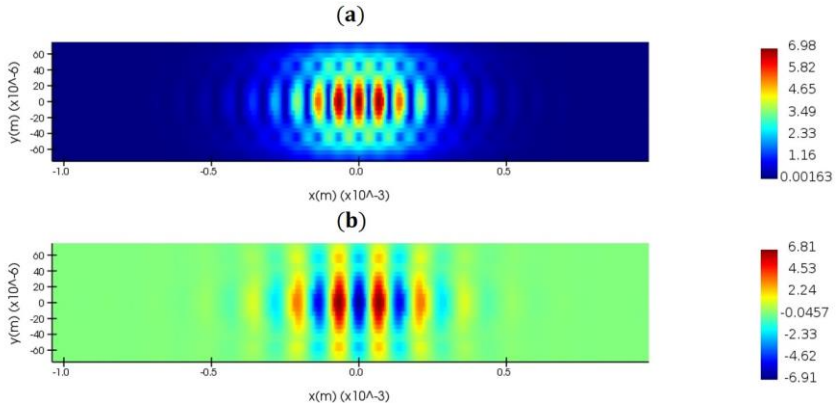


**Figure 4-8 (a) Magnitude of the electric field of 1 THz resonance mode in the x-y plane (b) Electric field of 1 THz resonance mode along the y-axis (along the width of waveguide) in the x-y plane**

As shown in Figure 4-8, the electric field is strong at the center of the cavity and lies mostly along the width of the waveguide; thus, it is appropriate to trap the generated THz wave to couple it to the waveguide. The field of resonance mode of the cavity at 1 THz is confined well between the Bragg mirrors. Because the quality factor of the cavity is high enough, confinement of field between the Bragg mirrors is effective, and the direction of the field for 1 THz resonance mode is along the width of the waveguide, this structure is appropriate for trapping the THz wave generated by the photoconductive source.

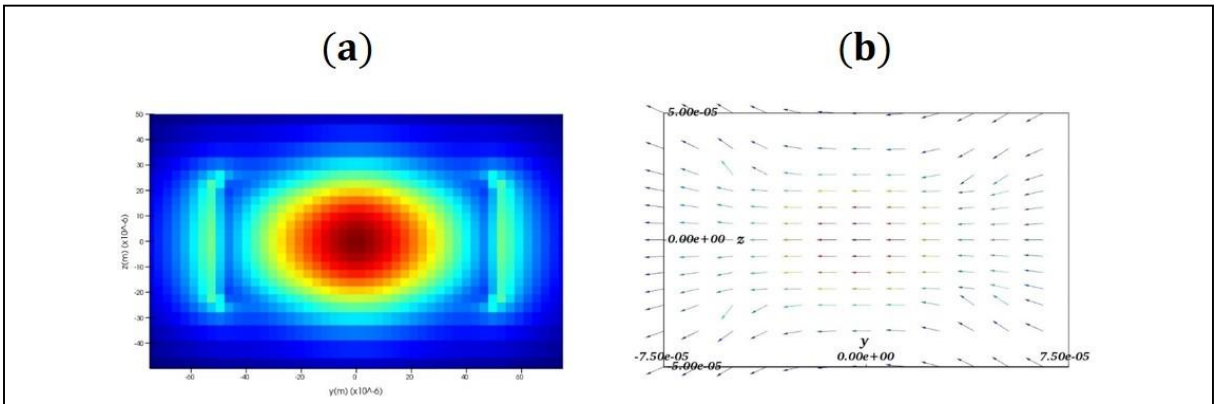


**Figure 4-9 (a) Magnitude of the electric field of 1 THz resonance mode in the cross-section of the waveguide (b) Vector of the electric field of 1 THz resonance mode in the cross-section of the waveguide**

As shown in Figure 4-9, the resonance mode of the cavity at 1 THz has an electric field the same as the $TE-like^{11}$ mode of the waveguide. Comparing Figure 4-9 to Figures 3-9 and 3-10, reveals that both fields in the cross-section of the waveguide are the same; hence, the mode of the cavity at 1 THz can couple to the waveguide by further design since they are the same mode.

## 4.4 Conclusion

In this chapter, after a short review on the cavities with a focus on photonic crystal nanobeam cavities, a photonic crystal nanobeam cavity has been analyzed. This cavity has a high quality factor of 1023 at the resonance frequency of 1 THz.

Since the electric field of the resonance mode of the cavity at 1 THz is along the width of the waveguide, this cavity is appropriate to trap the generated THz wave from the CW photoconductive source. Also, because the mode of the cavity in the cross-section of the waveguide is the same as the $TE-like^{11}$ mode of the waveguide, the THz wave will couple to the waveguide after the trapping by the cavity with further design.

# Chapter 5
# Conclusion

The main objective of this thesis has been to construct a structure for trapping and confining a THz wave. As discussed in Chapter 4, by applying 12 holes in each side of the cavity inside a well-designed THz waveguide, a resonance mode with a high quality factor of 1023 has been found. This resonance mode at 1 THz has the same mode field as the waveguide's fundamental mode, so the cavity named the photonic crystal nanobeam cavity is able to trap the generated THz electromagnetic field. Its mode field in the direction of field propagations shows that the field is well-trapped inside the cavity, and the high quality factor of the cavity is the result of effective confinement of the electromagnetic field.

The properties and details of the designed waveguide have been studied in Chapter 3. The waveguide has a low loss of 0.057 $\frac{\mathrm{dB}}{\mathrm{cm}}$, and a size of $45 \times 100\ \mu\mathrm{m}^2$ in the transverse plane. The waveguide is the core and basis of the cavity. Because of the unique properties of HR-Si in the frequency of THz, this material is the candidate for fabricating the waveguide and the cavity. The proposed structure and its design, simulation, and analysis are the main contributions of this thesis.

All the THz components are designed for a specific kind of excitation; hence, the procedure of THz generation needed to be studied, as described in Chapter 2. Among the diverse methods of THz generation, photoconductive sources have been studied in detail and found to be the best candidate for the excitation of the proposed cavity and waveguide. LT-GaAs has been chosen as the photoconductive material. My contribution in this part is first, solving the equations for the interaction of light and semiconductor photoconductive material, and providing a simple dipole model for the generated THz photocurrent.

In this thesis, different interesting physical phenomena are studied, but many exciting investigations remain to be done in the future, as listed below.

1. The fabrication and characterization of the proposed structure is an immediate future work. The fabrication process of the cavity is similar to the fabrication of the waveguide, which has been discussed in Chapter 3, but deposition of LT-GaAs on the top of the cavity is challenging.
2. The process of optical to THz conversion can be enhanced by using plasmonic structures inside the electrodes. By applying a plasmonic pattern inside the electrodes, the optical confinement of the optical field increases, thus enhancing the amplitude of generated photocurrent.
3. Finding the coupling efficiency of the photonic crystal nanobeam cavity to the designed waveguide is of special importance. Ways to increase efficiency might be another interesting future work to pursue.

# References

* References are written in the format of MLA format in Google Scholar.

[1] Thomson, David, et al. "Roadmap on silicon photonics." Journal of Optics 18.7 (2016): 073003.

[2] Ghafarian, Naimeh. "Graphene travelling wave amplifier for integrated millimeter-wave/terahertz systems." (2018).

[3] Xie, Jingya, et al. "A Review on Terahertz Technologies Accelerated by Silicon Photonics." Nanomaterials 11.7 (2021): 1646.

[4] Sengupta, Kaushik, Tadao Nagatsuma, and Daniel M. Mittleman. "Terahertz integrated electronic and hybrid electronic–photonic systems." Nature Electronics 1.12 (2018): 622-635.

[5] Safian, Reza, Galia Ghazi, and Nafiseh Mohammadian. "Review of photomixing continuous-wave terahertz systems and current application trends in terahertz domain." Optical Engineering 58.11 (2019): 110901.

[6] Saeedkia, Daryoosh, and Safieddin Safavi-Naeini. "Terahertz photonics: Optoelectronic techniques for generation and detection of terahertz waves." Journal of Lightwave Technology 26.15 (2008): 2409-2423.

[7] Yardimci, Nezih Tolga, and Mona Jarrahi. "Nanostructure-Enhanced Photoconductive Terahertz Emission and Detection." Small 14.44 (2018): 1802437.

[8] Burford, Nathan M., and Magda O. El-Shenawee. "Review of terahertz photoconductive antenna technology." Optical Engineering 56.1 (2017): 010901.

[9] Khabiri, Mehrnoosh. Characterization and Analysis of Continuous Wave Terahertz Photomixers. MS thesis. University of Waterloo, 2012.

[10] Lee, Yun-Shik. Principles of terahertz science and technology. Vol. 170. Springer Science & Business Media, 2009.

[11] Duvillaret, Lionel, et al. "Analytical modeling and optimization of terahertz time-domain spectroscopy experiments, using photoswitches as antennas." IEEE Journal of Selected Topics in Quantum Electronics 7.4 (2001): 615-623.

[12] Chuang, Shun Lien. Physics of photonic devices. John Wiley & Sons, 2012.

[13] Neshat, M., D. Saeedkia, and S. Safavi-Naeini. "On the behavior of the radiation field from large-aperture terahertz photoconductive Antenna under impulsive excitation." 2007 International workshop on Antenna Technology: Small and Smart Antennas Metamaterials and Applications. IEEE, 2007.

[14] Piao, Zhisheng, Masahiko Tani, and Kiyomi Sakai. "Carrier dynamics and terahertz radiation in photoconductive antennas." Japanese Journal of Applied Physics 39.1R (2000): 96.

[15] Khiabani, Neda. Modelling, design and characterisation of terahertz photoconductive antennas. The University of Liverpool (United Kingdom), 2013.

[16] Tani, Masahiko, Kwang-Su Lee, and X-C. Zhang. "Detection of terahertz radiation with low-temperature-grown GaAs-based photoconductive antenna using 1.55 μm probe." Applied Physics Letters 77.9 (2000): 1396-1398.

[17] Tan, Dawn TH, Pang C. Sun, and Yeshaiahu Fainman. "Monolithic nonlinear pulse compressor on a silicon chip." Nature communications 1.1 (2010): 1-6.

[18] Kondo, K., et al. "Temporal pulse compression by dynamic slow-light tuning in photonic-crystal waveguides." Physical Review A 91.2 (2015): 023831.

[19] Fülöp, J. A., et al. "Generation of sub-mJ terahertz pulses by optical rectification." Optics letters 37.4 (2012): 557-559.

[20] Zhang, Shuangyou, et al. "Terahertz wave generation using a soliton microcomb." Optics Express 27.24 (2019): 35257-35266.

[21] Khabiri, Mehrnoosh, Mohammad Neshat, and Safieddin Safavi-Naeini. "Hybrid computational simulation and study of continuous wave terahertz photomixers." IEEE Transactions on Terahertz Science and Technology 2.6 (2012): 605-616.

[22] Dexheimer, Susan L., ed. Terahertz spectroscopy: principles and applications. CRC press, 2017.

[23] Amarloo, Hadi, Nazy Ranjkesh, and Safieddin Safavi-Naeini. "Terahertz silicon–BCB–quartz dielectric waveguide: an efficient platform for compact THz systems." IEEE Transactions on Terahertz Science and Technology 8.2 (2018): 201-208.

[24] Amarloo, Hadi. "New Platforms for Terahertz Silicon Waveguides and Their Application in Absorption Spectroscopy." (2018).

[25] Akiki, Elias. Integrated SOI photoacoustic gas sensor at THz frequencies for food quality control application. Diss. Université de lille, 2021.

[26] Pozar, David M. Microwave engineering. John wiley & sons, 2011.

[27] Saleh, Bahaa EA, and Malvin Carl Teich. Fundamentals of photonics. john Wiley & sons, 2019.

[28] Virginia Diodes, Inc. https://vadiodes.com/en/products/straight-waveguides-tapers-horn-antenna-directional-couplers

[29] Kirby, P. L., et al. "Characterization of micromachined silicon rectangular waveguide at 400 GHz." IEEE microwave and wireless components letters 16.6 (2006): 366-368.

[30] Hu, Jiang, Shanyi Xie, and Yong Zhang. "Micromachined terahertz rectangular waveguide bandpass filter on silicon-substrate." IEEE microwave and wireless components letters 22.12 (2012): 636-638.

[31] Leong, Kevin MKH, et al. "WR1. 5 silicon micromachined waveguide components and active circuit integration methodology." IEEE Transactions on Microwave theory and Techniques 60.4 (2012): 998-1005.

[32] Reck, Theodore, et al. "Silicon micromachined waveguide components at 0.75 to 1.1 THz." 2014 39th International Conference on Infrared, Millimeter, and Terahertz waves (IRMMW-THz). IEEE, 2014.

[33] Nordquist, Christopher D., et al. "Properties of surface metal micromachined rectangular waveguide operating near 3 THz." IEEE Journal of Selected Topics in Quantum Electronics 17.1 (2010): 130-137.

[34] Engel, Andrew G., and Linda PB Katehi. "Low-loss monolithic transmission lines for submillimeter and terahertz frequency applications." IEEE transactions on microwave theory and techniques 39.11 (1991): 1847-1854.

[35] Dib, Nihad, and Linda PB Katehi. "Characterization of three-dimensional open dielectric structures using the finite-difference time-domain method." IEEE transactions on microwave theory and techniques 44.4 (1996): 513-518.

[36] Malekabadi, Ali, et al. "High-resistivity silicon dielectric ribbon waveguide for single-mode low-loss propagation at F/G-bands." IEEE Transactions on Terahertz Science and Technology 4.4 (2014): 447-453.

[37] Hanham, Stephen M., et al. "LED-switchable high-Q packaged THz microbeam resonators." IEEE Transactions on Terahertz Science and Technology 7.2 (2017): 199-208.

[38] Akiki, Elias, et al. "High-Q THz photonic crystal cavity on a low-loss suspended silicon platform." IEEE Transactions on Terahertz Science and Technology 11.1 (2020): 42-53.

[39] Ranjkesh, Nazy, et al. "Silicon-on-glass dielectric waveguide—Part I: For millimeter-wave integrated circuits." IEEE Transactions on Terahertz Science and Technology 5.2 (2015): 268-279.

[40] Ranjkesh, Nazy, et al. "Silicon-on-glass dielectric waveguide—Part II: For THz applications." IEEE Transactions on Terahertz Science and Technology 5.2 (2015): 280-287.

[41] Ranjkesh, Nazy, et al. "1.1 THz U-silicon-on-glass (U-SOG) waveguide: A low-loss platform for THz high-density integrated circuits." IEEE Transactions on Terahertz Science and Technology 8.6 (2018): 702-709.

[42] Amarloo, Hadi, and Safieddin Safavi-Naeini. "Terahertz line defect waveguide based on silicon-on-glass technology." IEEE Transactions on Terahertz Science and Technology 7.4 (2017): 433-439.

[43] Tsuruda, Kazuisao, Masayuki Fujita, and Tadao Nagatsuma. "Extremely low-loss terahertz waveguide based on silicon photonic-crystal slab." Optics express 23.25 (2015): 31977-31990.

[44] Dai, Jianming, et al. "Terahertz time-domain spectroscopy characterization of the far-infrared absorption and index of refraction of high-resistivity, float-zone silicon." JOSA B 21.7 (2004): 1379-1386.

[45] Chang, William SC. Fundamentals of guided-wave optoelectronic devices. Cambridge University Press, 2009.

[46] Liu, Jia-Ming. Photonic devices. Cambridge University Press, 2009.

[47] Ranjkesh, N., et al. "Broadband single-mode THz suspended silicon-on-glass waveguide." IEEE Microwave and Wireless Components Letters 28.3 (2018): 185-187.

[48] Deotare P.B., Loncar M. (2012) Photonic Crystal Nanobeam Cavities. In: Bhushan B. (eds) Encyclopedia of Nanotechnology. Springer, Dordrecht. https://doi.org/10.1007/978-90-481-9751-4_291

[49] Vahala, Kerry J. "Optical microcavities." nature 424.6950 (2003): 839-846.

[50] Yablonovitch, Eli. "Inhibited spontaneous emission in solid-state physics and electronics." Physical review letters 58.20 (1987): 2059.

[51] E. Yablonovitch and T. J. Gmitter, "Photonic band structure: the face-centered-cubic case," J. Opt. Soc. Am. A 7, 1792-1800 (1990)

[52] Joannopoulos, John D., et al. Photonic crystals. Princeton university press, 2011.

[53] Foresi, J. S., et al. "Photonic-bandgap microcavities in optical waveguides." nature 390.6656 (1997): 143-145.

[54] Deotare, Parag B. Nanobeam cavities for reconfigurable photonics. Diss. Harvard University, 2012.

[55] Yang, Da-Quan, et al. "Photonic crystal nanobeam cavities for nanoscale optical sensing: A review." Micromachines 11.1 (2020): 72.

[56] Deotare, Parag B., et al. "High quality factor photonic crystal nanobeam cavities." Applied Physics Letters 94.12 (2009): 121106.

[57] Stutzman, Warren L., and Gary A. Thiele. Antenna theory and design. John Wiley & Sons, 2012.

[58] Jackson, John David. "Classical electrodynamics." (1999): 841-842.

# Appendix A
# Dipole Radiation

Since the photoconductive source has been modeled as a simple dipole in Chapter 2, the radiation of this dipole is investigated here. First, the radiation of a time-harmonic source is determined, and then the radiation of an arbitrary time-domain source would find out.

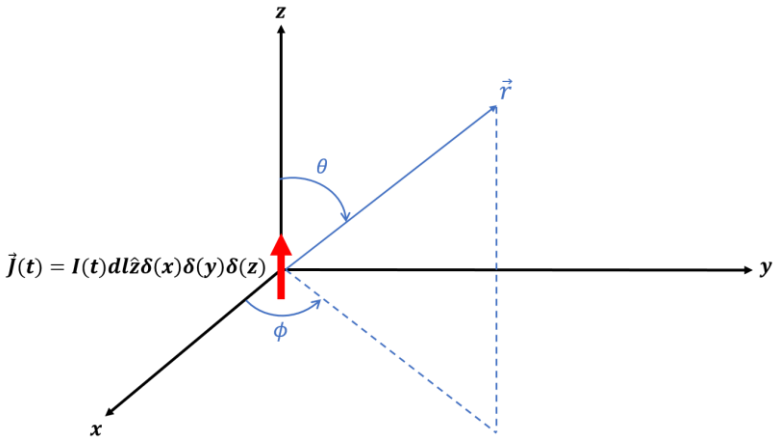


**Figure A-1 structure of a dipole toward z-axis at the center**

For a time-harmonic z-axis dipole ($Idl\hat{z}$) at the frequency of $\omega$:

$$\vec{A}(\omega) = \frac{\mu_0}{4\pi}\iiint_{current\ volume\ (v')} \vec{J}(\vec{r}',\omega)\frac{e^{-jk_0|\vec{r}-\vec{r}'|}}{|\vec{r}-\vec{r}'|}dv' \quad (A.1) \quad [57]$$

$$\vec{A}(\omega) = \frac{\mu_0 I(\omega)dl}{4\pi}\frac{e_0^{-jk_0 r}}{r}\hat{z} \quad (A.2)$$

$$\vec{E}(\omega) = \left(\frac{c^2}{j\omega}\right)\vec{\nabla}\times\vec{\nabla}\times\vec{A}(\omega) = E_r(\omega)\hat{r} + E_\theta(\omega)\hat{\theta} \quad (A.3)$$

$$E_r(\omega) = \frac{I(\omega)dl}{j2\pi\omega\epsilon_0}\left(\frac{1}{r}+jk_0\right)\frac{e^{-jk_0 r}}{r^2}\cos(\theta) \quad (A.4)$$

$$E_\theta(\omega) = \frac{-jI(\omega)dl}{4\pi\omega\epsilon_0}\left(\left(\frac{1}{r}+jk_0\right)^2 - \frac{jk_0}{r}\right)\frac{e^{-jk_0 r}}{r}\sin(\theta) \quad (A.5)$$

In this case, the far-field region is $r \gg \frac{\lambda}{2\pi}$ and the near-field is $r \ll \frac{\lambda}{2\pi}$.

To find out the time-domain answer, an inverse Fourier transform from A.4 and A.5 would cause the radiated electric field over time.

$$E_r(t) = \frac{dl}{2\pi\epsilon_0 r^2}\left(\frac{\int_0^{t-\frac{r}{c}} I(\tau)d\tau}{r} + \frac{I\left(t-\frac{r}{c}\right)}{c}\right)\cos(\theta) \quad (A.6)$$

$$E_\theta(t) = \frac{dl}{4\pi\epsilon_0 r}\left(\frac{1}{rc}I\left(t-\frac{r}{c}\right) + \frac{1}{c^2}\frac{d}{dt}I\left(t-\frac{r}{c}\right) + \frac{\int_0^{t-\frac{r}{c}} I(\tau)d\tau}{r^2}\right)\sin(\theta) \quad (A.7)$$

For far-field, the dominant term would be $\frac{1}{r}$ and for the near-field dominant term is $\frac{1}{r^3}$.

$$\vec{E}^{far-field}(t) = \frac{dl}{4\pi\epsilon_0 c^2 r}\frac{d}{dt}I\left(t-\frac{r}{c}\right)\sin(\theta)\,\hat{\theta} \quad (A.8)$$

Due to A.8, the far-field electric field is relative to the derivative of the current.

$$Idl = \frac{dp}{dt} \rightarrow \vec{E}^{near-field}(t) = \frac{p\left(t-\frac{r}{c}\right)}{4\pi\epsilon_0 r^3}\left(2\cos(\theta)\,\hat{r} + \sin(\theta)\,\hat{\theta}\right) \quad (A.9)$$

Equation A.10 is the same as the electric field of an electric dipole at the center and the term of $\frac{r}{c}$ is proportional to the spatial delay of electromagnetic radiation.

By the assumption of moving a charge $q$ along z with the acceleration of $a$ the radiated power can be calculated.

$$Idl = qv \rightarrow \vec{E}^{far-field} = \frac{qa}{4\pi\epsilon_0 c^2 r}\sin(\theta)\,\hat{\theta} \quad (A.10)$$

$$\vec{S}(t) = \frac{1}{\eta_0}E(t)^2\,\hat{r} = \frac{1}{\eta_0}\left(\frac{qa}{4\pi\epsilon_0 c^2 r}\sin(\theta)\right)^2\hat{r} \quad (A.10)$$

$$P(t) = \int_0^{2\pi} \int_0^{\pi} Sr^2 \sin(\theta)\, d\theta d\phi = \frac{q^2 a^2}{6\pi\epsilon_0 c^3} \quad (A.11)$$

Equation A.11 is Larmor's formula found in [58] and describes the radiation of a moving charge.

For a dipole current source at the frequency $\omega$ and amplitude of $I\_A$, its average power and its electric field over time are calculated in A.13 and A.12.

$$\vec{E}^{far-field}(\omega) = \frac{j\omega\mu_0 I(\omega) dl}{4\pi} \frac{e^{-jk_0 r}}{r} \sin(\theta)\, \hat{\theta} \quad (A.12)$$

$$P_{average} = \frac{k_0^2 dl^2 \eta_0 I_A^2}{12\pi} \quad (A.13)$$